UiO : Institute of Theoretical Astrophysics
University of Oslo

3D Radiative Transfer on Irregular Grids

Magne Elias Roland Udnæs
Master's Thesis, Spring 2022

Abstract

Three-dimensional radiative transfer calculations involve extensive amounts of computation. These calculations are done on three-dimensional model atmospheres where the MHD equations are solved. Typically, model atmospheres are run on a discretised Cartesian grid, which is often not ideal for detailed calculation of spectral lines. This thesis investigates radiative transfer on irregular grids to improve spectral line calculations.

In one-dimensional radiative transfer, optimised grids lead to an accelerated convergence in solving the radiative transfer equation iteratively. These optimised grids are partitioned unevenly, and extending such grids to three dimensions requires different ray tracing methods than the traditional long and short characteristics. In this thesis, I develop a ray tracing algorithm on irregular grids. I construct a Voronoi diagram on the irregular grid and trace rays along its Delaunay lines. This ray tracing method gives good results in the searchlight beam test, producing similar amounts of diffusion as the short characteristics method with a piecewise linear interpolation.

The irregular grid framework is extended to a two-level atom problem in a quiet Sun MHD simulation. On a reduced resolution of the atmospheric model, the quality of synthesised spectra calculated with irregular grids is not as good as that of the Cartesian grid. However, optimised irregular grids converge nearly twice as fast as regular Cartesian grids. Although these calculations are modest with grid points, I also expect an accelerated convergence for higher resolution calculations.

This work establishes irregular grids' capability to calculate three-dimensional radiative transfer in the solar atmosphere. Further improvement to the methods can make NLTE calculations on irregular grids more fitting than on Cartesian grids.

Acknowledgments

First and foremost, I want to acknowledge my supervisor, Tiago. Thank you for helping me, giving valuable input to my work, and being the best supervisor I could ask for. I would also like to extend my gratitude towards my cosupervisor Mats, for helping me with staking out the direction of this thesis.

As every other thing in this life, nothing would be possible without our origin. However, it is not my existence I wish to address. Instead, I want to express my gratefulness for the support I have received from my parents through the entire process that constitutes my thesis. My sisters and brother were also great to have around these past years. Thank you all for giving feedback on my writing, including Elling and Stian.

To my fellow master students: thank you for two great years, they would not be the same without the long lunch breaks or the trips to bunnpris.

Last, my partner Elin. Thank you for being by my side through this process.

Contents

List of Figures

Chapter 1

Introduction

Throughout the last centuries, great attention has been given to studying the light that comes from the Sun. Physical processes within the Sun imprint small clues on the solar radiation that we observe at Earth. The spectrum spanned by this radiation holds the key to our life-giving star's inner mechanics.

Within large parts of the Sun, the matter is in thermal equilibrium. In 1900, German physicist Max Planck derived a formula describing how black bodies in thermal equilibrium emit radiation. This formula depends on temperature only; therefore, the radiation emitted from perfect black bodies sheds little light on the physical processes inside the body. Observing radiation from black bodies solely provides insight into the temperature where radiation is formed. Fortunately, the Sun is not a perfect black body. While observations of the Sun mimic Planck's distribution, essential deviations are imprinted in the spectrum. Understanding these deviations unlocks the secrets of the Sun.

At the beginning of the 19th century, a deviation from the black body spectrum coming from the Sun was observed for the first time.[1] The deviation came from atoms in the solar atmosphere absorbing and emitting photons. This kind of deviation—arguably the most important kind of deviation from the black body spectrum—is called a spectral line. Plenty spectral lines exists, either in emission or absorption from the black body continuum depending on the physical conditions where they form.

A thin envelope of gas surrounding the dense interior of the Sun forms the spectral lines in the solar spectrum. This low-density region extends millions of metres above the solar surface. It is the solar atmosphere. Coupling the physical conditions in the solar atmosphere to the spectral lines that we observe is not an easy task—it requires extensive computational resources. Only in later years technology has made it viable to model the atmospheric conditions of the Sun realistically.

[1] William Wollaston observed absorption lines from the solar spectrum in 1802. These were the Ca II h & k and Na I D lines.

Even though fluid simulations of the Sun have been fruitful, a detailed three-dimensional description of radiative transfer in the solar atmosphere is still lacking for many spectral lines. Until recently, detailed spectral synthesis has been available in one dimension only. Three-dimensional calculations have been restricted by the intricacy of modelling radiation in dynamic conditions where mass density varies over orders of magnitude.

Classically, well established numerical schemes in one dimension have been used to synthesise spectral lines.[2] The numerical scheme in question is an implicit solver that iterates towards the correct solution of the radiation field. These one-dimensional radiative transfer solvers have accurately reproduced spectral lines from the Sun. However, there are observations that one-dimensional calculations fail to synthesise. Several physical processes important for line formation are impossible to model in 1D. Three-dimensional effects such as macroscopic Doppler shifting due to a moving fluid is one quantity that cannot be treated correctly in 1D. The Magnetic field is another inherently three-dimensional quantity important for line formation. For example, the important spectral diagnostic Hα needs a three-dimensional treatment because "the presence of magnetic fields leads to structures that cannot be reproduced in one-dimensional (1D) or two-dimensional (2D) modeling" (Leenaarts et al., 2012).

The requirement for three-dimensional radiative transfer calculation is apparent. However, there are several inhibiting factors in existing methods. Olson et al. (1986) note that spectral synthesis on fine grids converges slower in one dimension; the extension to 3D is worse. The computational complexity of calculating multilevel atoms with high spatial resolution is not feasible. Alas, high resolution radiative transfer is necessary to compare synthesised lines with observations from the next-generation solar telescopes, like the recently operational DKIST or the planned EST.[3]

While efforts have been made to optimise grids for better convergence in one-dimensional radiative transfer calculations of the solar atmosphere, a three-dimensional counterpart is lacking. This absence comes partly because ray tracing algorithms for three-dimensional irregular grids are slower than their Cartesian counterparts. Still, such algorithms have been developed for studies of astrophysical systems other than the Sun. An example of this is Camps et al. (2013), who use a Voronoi tessellation to calculate radiation in galactic structures. They conclude that "the benefits of using a Voronoi grid in radiative transfer simulation codes will often outweigh the somewhat slower performance". Making an irregular grid enables a finer resolution in areas more sensitive to radiation, while simultaneously having a coarser resolution in less important areas. The irregular grid could bring two large benefits: the first coming as a quicker convergence of the Λ-iteration; the second being increased spatial resolution of sensitive

[2] The traditional method is called Λ-iteration. With the combination of a technique called operator splitting technique, this method has proven an effective tool in one-dimensional radiative transfer.

[3] DKIST (short for *Daniel K. Inouye Solar Telescope*), is a four-meter telescope capable of studying "features as small as 35 kilometres across" (Witze, 2020). The EST (shorthand for *European Solar Telescope*) is a project that has been long in the planning. While its primary mirror is not planned to be larger than DKIST's, the EST would provide diagnostics to understand the magnetic fields and plasmas in the solar atmosphere.

regions without using more grid points in calculations.

Considering the potential benefits an optimised grid can have for three-dimensional radiative transfer calculations, I realised the importance of an investigation into the subject. Improving three-dimensional radiative transfer is crucial for two reasons: the next generation of solar telescopes will reveal small scale details in the spectra of the Sun, requiring higher resolution spectral synthesis comparison; and, several spectral lines are not yet viable to model in 3D due to computational limitations imposed by physical complexity.

The transition from regular to non-regular grids introduces several obstacles. Additional book-keeping and slower performance are expected. However, finding proper solutions to these challenges can stake the direction toward improved three-dimensional radiative transfer calculations.

Chapter 2

Background

2.1 The radiative transfer equation

The radiative transfer equation (RTE) describes intensity along a ray in a medium. It is dependent of the path s light travels, time t, and expressed at a wavelength λ as

$$\left[\frac{1}{c}\frac{\partial}{\partial t} + \frac{\partial}{\partial s}\right] I_\lambda(s,t) = -\alpha_\lambda(s,t) I_\lambda(s,t) + j_\lambda(s,t)\,. \tag{2.1}$$

Here, $\alpha_\lambda(s,t)$ is the extinction coefficient, $j_\lambda(s,t)$ is the emissivity, and c is the speed of light.

The extinction coefficient α_λ accounts for the removal of energy—or the number of photons—from the ray, either through absorption or scattering processes. Extinction is defined per unit path length.

Emissivity is the addition of energy or photons to the ray from emission processes. It has the same units as intensity, divided by unit length.

In the solar atmosphere, the photon free flight time is much smaller than any timescale in the variation of the fluid. It is "of the order of seconds" (Stein & Nordlund, 1998), resulting in a rapid stabilisation of the radiation field after any change in the fluid. Consequently, the intensity I_λ has no time-dependence that is not introduced by the fluid. Given that we know how the atmosphere looks like at a time t, the partial derivative of I_λ with respect to time in Equation (2.1) can be neglected.

Instead of using the physical length unit s, it is common to use optical depth. This refers to the path light experiences. The monochromatic optical depth increment $\mathrm{d}\tau_\lambda$ is given by the extinction coefficient and path length as

$$\mathrm{d}\tau_\lambda(s) \equiv -\alpha_\lambda \mathrm{d}s\,. \tag{2.2}$$

The optical depth can then be found by integrating Equation (2.2):

$$\tau_\lambda(s) = \int_s^0 \alpha_\lambda(s)\mathrm{d}s\,. \tag{2.3}$$

While a single photon can travel any distance in optical depth before interacting with the medium, an ensemble of photons obey statistical laws. The mean path length a photon travels is

$$\langle\tau_\lambda\rangle = 1\,. \tag{2.4}$$

Another useful quantity for radiative transfer is the source function S_λ. The source function describes the ratio of emission to extinction, and is defined as

$$S_\lambda \equiv \frac{j_\lambda}{\alpha_\lambda}\,. \tag{2.5}$$

The source function can be a brilliant quantity to introduce. Major benefits of this quantity come from its compactness and utilisation in an algorithm called Lambda iterations that is introduced and used later in this thesis. It should, however, be treated with care. Behind this seemingly simple term lies a great deal of complicated physics requiring advanced comprehension of the microscopic processes taking place in the fluid of the Sun.

Using the quantities described above, dropping the time-dependence, and recasting the transport equation in terms of optical depth, the Equation (2.1) transforms to

$$\frac{\mathrm{d}I_\lambda}{\mathrm{d}\tau_\lambda} = S_\lambda - I_\lambda\,. \tag{2.6}$$

This is the simplest form of the transport equation, although it carries a manifold of details.

2.1.1 The formal solution

Integrating the time-independent transport equation in Eq. (2.6) by the integrating factor $\exp(\tau_\lambda)$, one obtains the *formal solution* to the Radiative Transfer Equation:

$$I_\lambda(\tau_\lambda) = I_\lambda(0)e^{-\tau_\lambda} + \int_0^{\tau_\lambda} S_\lambda(\tau'_\lambda)e^{-(\tau_\lambda-\tau'_\lambda)}\,\mathrm{d}\tau'_\lambda\,. \tag{2.7}$$

The advantage of the formal solution is that it "lives" in one dimension, making it simple to calculate radiation when the source function is known. The drawback is that the source function is known only *a priori* in constructed problems. The source function is elusive in physical media, mainly due to scattering processes. Finding the source function is the essence of numerical radiative transfer calculations of the Sun.

2.2 From 1D to 3D radiative transfer

In three dimensions, the radiative transfer equation depends on the direction of the beam under consideration. The angular integration of the intensity field gives rise to the quantity called angle-averaged (or mean) intensity. Denoted J_λ and dependent on wavelength and position, we calculate it as the integral of intensities over solid angle at optical depth τ_λ,

$$J_\lambda(\tau_\lambda) = \frac{1}{4\pi} \int_0^{2\pi} \int_0^{\pi} I_\lambda(\tau_\lambda) \sin(\theta) \, \mathrm{d}\theta \mathrm{d}\phi \, . \tag{2.8}$$

In many models, atmospheric variables depend solely on height—a semi-infinite plane-parallel atmosphere. These problems reduce to one dimension, but the mean intensity is still an important quantity. For the sake of completeness, I include methods for 1D radiative transfer. These methods are highly developed and provide the basis for expanding to 3D. In 1D, we find the mean intensity by integrating specific intensity over the inclination of the ray,

$$J_\lambda(\tau_\lambda) = \frac{1}{2} \int_{-1}^{1} I_\lambda(\tau_\lambda, \mu) \mathrm{d}\mu \, , \tag{2.9}$$

where the inclination is defined as

$$\mu = \cos\theta \, . \tag{2.10}$$

The continuous integral calculating mean intensity can be solved as a quadrature over rays,

$$J_\lambda(\tau_\lambda) \approx \sum_i \omega_i I_{\lambda,i}(\tau_{\lambda,i}) \, , \tag{2.11}$$

making the problem discrete. To obtain an accurate result, we should sample rays carefully over the unit sphere. Since the problem is solved over rays, parts of the problem are effectively reduced to one dimension. For each ray, the formal solution is used to calculate intensity.

The approach of discretising rays over several solid angles is called the method of characteristics. Originally named the S_n-method, the method of characteristics was first devised at Los Alamos (e.g. Carlson, 1955), and later developed by Keller & Wendroff (1957).

In 1D radiative transfer, the discretised rays will strike the same cell centres for every inclination. This property of one-dimensional radiative transfer makes it very accessible to distribute grid points beneficially for calculations, optimising the grid for radiative transfer. For example, Carlsson (1986) optimises the computational grid by placing depth points such that the maximum difference in optical depth is constant for each column of a model atmosphere, i.e. $\max(\Delta \log_{10} \tau) \equiv$ constant.[1] Later, Carlsson &

[1] The depth optimisation found in MULTI is provided by Jaime de la Cruz Rodriguez as open-source software in the GitHub repository https://github.com/jaimedelacruz/depthOptimizer, with some extension to the original algorithms.

Stein (1992) use an adaptive mesh for 1D radiative transfer calculations to "resolve the regions where the atomic level populations are changing rapidly". The scheme was inspired by Dorfi & Drury (1987), who find that "Simple Adaptive Grid Equations [...] constitutes a valuable technique for the numerical solution". Although Dorfi & Drury (1987) test these techniques on hydrodynamic equations, the argument is that an adaptive mesh gives better results for all systems varying over orders of magnitude—as is the case for radiative transfer calculations in the solar atmosphere.

While depth optimisation works well for one-dimensional radiative transfer, the story is different when we take the step to three dimensions. In this higher-dimensional space, the discretised rays in the method of characteristics will traverse the grid in different arrangements for every solid angle. Accordingly, depth optimisation breaks down in three dimensions. To understand why it is difficult to optimise a three-dimensional grid for radiative transfer, I introduce the standard methods for traversing rays in the characteristic methods in 3D.

2.2.1 Long characteristics

Much work on the method of characteristics was done in simplified two- and three-dimensional geometries (see review by Crosbie & Linsenbardt, 1978), however the formal definition of the long characteristics method (also denoted LC), was presented in a series of papers by Jones and Skumanich, (see Jones, 1973; Jones & Skumanich, 1973).

The long characteristics method starts at a grid point, and traces a ray backwards through the entire medium under consideration, until one of the boundaries is reached. Thus the incident intensity I_0 of Equation (2.7) is always equal to one of the boundary conditions. Along the ray, we solve the integral of the formal solution sequentially. The ray will (in general) not strike the grid points in each layer, involving interpolation of the source function and extinction coefficient.

The rays in the LC have to propagate backwards through $N - l$ layers of the model, where l is the layer the ray is intersecting. This way of propagating rays until the border for every grid point, gives the LC method $\mathcal{O}(N)$ calculations per grid point. In a three-dimensional grid with N^3 grid points, the computational complexity of the LC method is $\mathcal{O}(N^4)$—a high price to pay.

2.2.2 Short characteristics

Even though the LC method gives good accuracy, it is not a good choice for large simulations due to its high computational complexity. The short characteristics (SC) method, developed by Kunasz & Auer (1988), amends this problem. Short characteristics traces rays between neighbouring grid points only. It propagates rays starting from a boundary of the domain to the next immediate layer, from this layer to the next one, and so on. The calculation of the formal solution uses two values per grid point, making the method scale with the total number of grid points. The SC method,

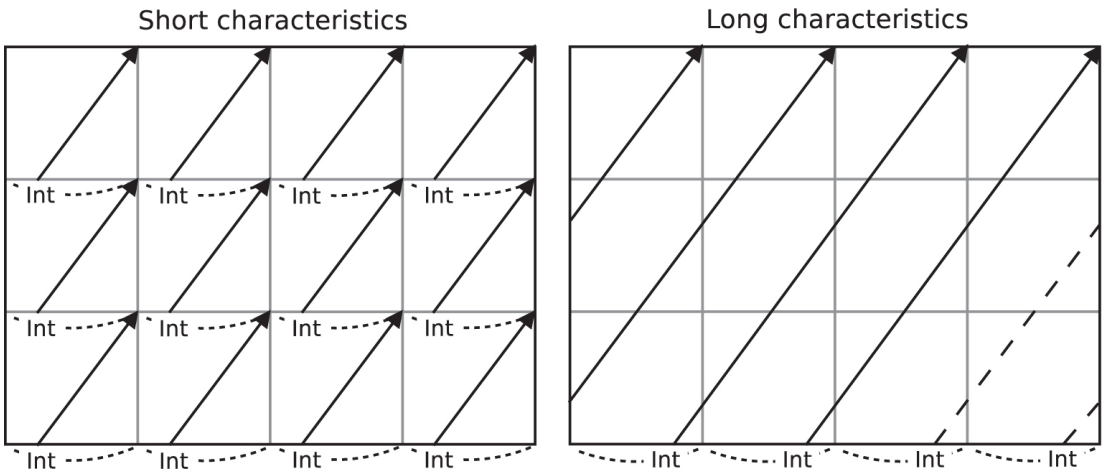

Figure 2.1: Two-dimensional comparison between long and short characteristics, showing "propagation strategy to compute the radiation emerging at the top plane with the SC and the LC methods". Locations where interpolation of I_0 in Equation (2.7) is necessary are marked with "Int". Figure adapted from de Vicente et al. (2021), reproduced with permission of the authors.

therefore, has a computational complexity following $\mathcal{O}(N^3)$, where N is the number of grid points per axis.

Although the SC method is much better than LC in terms of computational intensity, this improvement comes with a sacrifice. Where the LC method only needs to interpolate I_0 at the boundaries, the SC method has to interpolate I_0 at every grid layer. Interpolations make the SC method more diffusive, and the diffusion increases for every layer away from the boundary.

The difference between the LC and SC methods is epitomised in figure 2 of de Vicente et al. (2021), that is repeated here in Figure 2.1.

Both the LC and SC methods require a regular grid, making it challenging to optimise depth points consistently for every solid angle ray in the angular quadrature (2.11). This obstruction advocates a new method to trace rays through a three-dimensional domain, that can consider an optimisation of grid points for every solid angle. Understanding how the RTE is solved makes it possible to guess how grid points should be distributed to optimise the grid for radiative transfer. The subsequent section discusses the solution scheme.

2.2.3 Λ-iterations

In stellar atmospheres, a process complicates any direct solution of the radiative transfer equation and promotes implicit solution techniques. This process is scattering.

Scattering occurs when a radiatively excited atom deexcites through a spontaneous

or induced deexcitation. If the mass density in a medium is low, collisions between particles are relatively rare. Here, natural (induced or spontaneous) deexcitation is far more likely to occur in an excited ion. Photons are absorbed and re-emitted by the medium—they are scattered. Scattering can occur several times before a photon is destructed. In the thin parts of the solar atmosphere, scattering dominates atomic transitions.

In optically thin regions, photons can travel very far before being destructed. Consequently, the energy photons carry is deposited very far from where the photon was created. Photons transport energy over long distances, couple distant locations in the medium to each other, and make the source function dependent on both the local conditions and the global radiation field. In scattering regions, an approximation of the source function is the combination of a scattering term and a thermal term:

$$S_\lambda(J_\lambda, T) = (1 - \varepsilon_\lambda)J_\lambda + \varepsilon_\lambda B_\lambda(T)\,. \tag{2.12}$$

Here ε_λ is the photon destruction probability, J_λ is the mean radiation field, and B_λ is the thermal radiation. If the photon destruction probability is equal to one, then there is no scattering, and we can see that the source function reduces to the thermal term, which is the Planck function. In this case, the system is said to be in local thermal equilibrium (LTE). For all other cases, there is scattering present, and the system is in non-LTE (NLTE).

The source function in Equation (2.12) depends on the mean intensity field J_λ, which in turn depends on S_λ through Equation (2.8). This implicit relation prohibits any analytic solution of the radiative transfer equation. Instead, the RTE is solved by introducing the Lambda operator. The Lambda operator is defined as

$$J_\lambda = \Lambda\left[S_\lambda\right]\,, \tag{2.13}$$

and introduced to Equation (2.12), altering the source function to look like

$$S_\lambda = (1 - \varepsilon_\lambda)\Lambda\left[S_\lambda\right] + \varepsilon_\lambda B_\lambda\,. \tag{2.14}$$

This expression gives the basis for the Λ-iteration algorithm. The source function can be solved by inverting the problem, giving the direct solution

$$S_\lambda = \left(1 - (1 - \varepsilon_\lambda)\,\Lambda\right)^{-1}\left[\varepsilon_\lambda B_\lambda\right]\,. \tag{2.15}$$

While this solution is mathematically simple to construct, the matrix inversion can be non-viable to compute. The solution is non-local, meaning that the Λ-matrix contains many elements far from the diagonal (similar to saying that the matrix has a large bandwidth). Non-locality in the system makes the full Λ-matrix very hard to invert. In 3D on a grid with N^3 grid points the computation scales as N^9 (Rutten, 2003). A Λ-matrix with diagonal elements only, is similar to the physical system being in LTE, where the solution is trivial. In our case however, this non-locality means that we are in NLTE and should try different schemes to solve the source function.

Instead of inverting the matrix in (2.15), the system can be solved iteratively with Equation (2.14). Iterating betters the prospects in terms of computational intensity. Since computing the source function in the latter equation requires $\mathcal{O}(N^3)$ calculations only, the iteration scheme scales as $n_{\text{it.}}N^3$, where $n_{\text{it.}}$ is the number of iterations the solution requires to converge.

The Λ iteration starts with an initial guess of the source function. One possibility is to start in LTE, i.e.

$$S_\lambda^{(0)} = B_\lambda \,.$$

The simplest Λ scheme advances by

$$S_\lambda^{(n+1)} = (1-\varepsilon_\lambda)\,\Lambda\left[S_\lambda^{(n)}\right] + \varepsilon_\lambda B_\lambda \,, \tag{2.16}$$

and the iterations are performed until the criterion

$$\max_\lambda \left[\text{abs}\left(1 - \frac{S_\lambda^{n+1}}{S_\lambda^n}\right)\right] < \epsilon \,, \tag{2.17}$$

is fulfilled (typically $\epsilon \leq 10^{-3}$), or a number of max iterations is reached where it is said that the solution did not converge.

In complex model atmospheres that contain regions with high optical depth and strong scattering, this naive iteration scheme fails. The source function will instead stabilise at the wrong solution, an artefact brought by the destruction factor ε_λ being small when there is strong scattering. We can see from Equation (2.14) that the correction of the source function is minimal per iteration in this scenario. This fact is reinforced in Rybicki & Hummer (1991): "each cycle of the iteration corresponds to photons moving about one free path of the medium" (the mean free path is closely related to the inverse square root of ε_λ). Per Rutten (2003, p. 124), the solution converges in "$1/\varepsilon$ for a Gaussian line and of order $1/\varepsilon^2$ for a Lorentzian".

It is common to employ operator splitting to solve the convergence problem of Λ-iterations. First introduced in stellar context by Cannon (1973)—who separate an approximate operator Λ^* from the exact Λ operator—the operator splitting technique significantly speeds up convergence in scattering media. For one-dimensional radiative transfer codes, several operator splitting techniques have been successful in solving multilevel NLTE problems.[2]

Extending Λ-iterations to 3D, it is natural to apply the local operator (Olson et al., 1986) to accelerate convergence. However, expecting similar convergence properties as 1D multilevel NLTE problems will lead to disappointment. In three dimensions, radiative transfer codes tend to suffer from slow convergence (e.g. a hydrogen atom model that uses more than 800 iterations to converge in Bjørgen & Leenaarts, 2017, fig. 12).

[2] E.g. the core saturation approximation defined by Scharmer (1981), or the local operator from Olson et al. (1986), which is easy to extend to higher dimensions.

2.3 Extinction and emission

Extinction and emission are already defined as α_λ and j_λ, but not much attention has been given to the microscopic processes encompassed within these quantities. These processes occur due to interactions between photons and particles.

Both processes are wavelength dependent: interactions with particles depend on the energy the photons carry. This dependence comes from atoms comprising different energy levels and wavelength-dependent scattering processes stemming from the wave-particle duality of ions.

The processes are split into two principal groups: continuum and line processes. The continuum processes are interactions that happen for a broad range of wavelengths, encompassing bound-free and free-free interactions between photons and particles, and elastic scattering processes. The line processes involve the discrete energy levels of atoms. Also called bound-bound processes, line processes are discrete and occur only for specific wavelengths.

2.3.1 Bound-bound transitions

An atomic bound-bound transition happens when an electron transitions between two different energy levels within an atom. The transition between an upper level u and a lower level l of an atom with energy difference χ may occur in five ways.

Radiative excitation takes place when a photon excites the atom from a lower level l to an upper level u. The rate of this transition is $B_{lu}\bar{J}^{\varphi}_{\lambda_0}$, given in "number of radiative excitations from state l to state u per sec per particle in state l" (Rutten, 2003, p. 21). B_{lu} is the Einstein coefficient for the transition, and $\bar{J}^{\varphi}_{\lambda_0}$ is the mean intensity field weighted over the extinction profile $\varphi(\lambda - \lambda_0)$.

Induced deexcitation is also a bound-bound transition involving photons. Also referred to as stimulated emission, this process occurs when a photon is in the vicinity of an excited atom. This "disturbance" from the photon can make the atom deexcite and emit a photon. The transition rate $B_{ul}\bar{J}^{\chi}_{\lambda_0}$ is the "number of induced radiative deexcitations from state u to state l per sec per particle in state u" (Rutten, 2003, p. 22). B_{ul} is the Einstein coefficient for the transition, and $\bar{J}^{\chi}_{\lambda_0}$ is the mean intensity field weighted over the stimulated emission profile $\chi(\lambda - \lambda_0)$.

Spontaneous deexcitation happens when the atom naturally deexcites from an excited state without any external stimulus. Due to the instability (finite lifetime) of excited states, the atom may at any time spontaneously deexcite from the upper level u to the lower level l, emitting a photon. This process happens independently of any radiation field, with the rate A_{ul} (per sec per particle in state u).

Collisional excitation. In a populated medium, collisions between the atom and other particles are frequent. During collisions, kinetic energy can be converted to the potential

energy of the atom, exciting it to level u. The Einstein collisional coefficient is C_{ul}, number of collisional excitations from state l to state u per sec per particle in state l.

Collisional deexcitation is the opposite process of collisional excitation. An atom colliding with another particle can deexcite the atom from state u to l, transferring the energy difference to kinetic energy. The rate for this transition is C_{lu}.

These processes contribute to the spectrum around the wavelength $\lambda_0 = hc/\chi$, creating a *spectral line*. Again, χ is the energy difference between two distinct and discrete energy levels in an atom.

2.3.2 Bound-free transitions

Bound-free transitions involve either ionisation or recombination of an ion with an electron. The electron transitions from a bound to a free state, or inversely from a free to a bound state. Just like a bound-bound transition, bound-free transitions can happen in five ways. These five ways are included in collisional, radiative, and spontaneous processes. The difference between these transitions and the bound-bound transitions, is that the upper level u of the transition is the ionised stage. This stage is also called the continuum. Bound-free processes can be split into two cases.

The first case is the ionisation of an atom. When an atom is ionised, it can happen in two ways. It is either ionised from a collision with a high kinetic energy particle or a high energy photon. If a collision is to ionise an atom, the kinetic energy of the particle it collides with needs to be higher than the ionisation potential of the atom, χ_∞. The same applies to ionisation by a photon with wavelength λ. The atom's ionisation energy can be converted to wavelength, imposing an upper wavelength boundary for ionisation. Thus photons need a wavelength that satisfies $\lambda < hc/\chi_\infty$ to ionise the atom. Collisional ionisation happens with a rate C_{lu}, similar to the bound-bound collisional excitation; however, the radiative ionisation's rate is slightly different. It is not integrated over the line profile, but rather the ionisation profile, $B_{lu}\bar{J}^{\varphi}_{\lambda_0}$.

In the second case, a free electron recombines with an atom. This process has three variations, which can happen either through spontaneous, induced, or collisional recombination. Spontaneous recombination can take place in an ion-electron collision. Induced recombination happens in a collision between an ion, electron and a photon, while collisional recombination happens in a collision between an ion, electron, and a third particle.

2.3.3 Free-free transitions

The free-free processes are better known by the German name *Bremsstrahlung*, translated to breaking radiation. Bremsstrahlung is produced when an electron (or another charged particle) decelerates. This is why the term *free-free* is used for the process: the particle is in a free state both before and after radiation is emitted.

2.3.4 Elastic processes

The last processes outlined here are processes in which photons scatter directly with electrons. These scattering processes are coherent and change the direction of the photon only. The energy of the incoming photon is the same as that which is emitted; hence the term *elastic*—energy is conserved. A well-known elastic scattering process is Rayleigh scattering. This process scatters photons by bound electrons when the photon wavelength is much longer than the characteristic wavelength of the electrons' binding energy. Another scattering process is significant for stellar atmospheres abundant with ionised hydrogen. Here, a major source of continuous extinction is Thomson scattering. This scattering mechanism of photons by free electrons is independent of wavelength, with extinction coefficient

$$\alpha^T = \sigma^T N_e \,, \tag{2.18}$$

where N_e is the electron density, and $\sigma_\nu^T = 6.65{\cdot}10^{-25}$ cm^2 is the extinction cross-section per electron.

2.3.5 Extinction and emission profiles

Extinction and emission profiles describe how radiation is absorbed or emitted from atoms. For a stationary atom with an infinite lifetime of the atomic levels, the profile will be a delta function centred at the energy difference between the levels. There are, however, no spectral lines shaped like this; spectral lines are smeared out over a range of wavelengths. This smearing is caused by several processes associated with the term broadening.

One of the main processes responsible for line broadening is temperature. Microscopic particles' motions in a fluid create small Doppler shifts with respect to the rest frame. The result is a broadening to the wavelength distribution of absorbed and emitted photons. This kind of broadening is called *thermal broadening*. In a Maxwellian velocity distribution, the thermal broadening can be quantified. It assumes the shape of a Gaussian profile. The extinction profile given by pure thermal broadening is

$$\varphi(\lambda - \lambda_0) = \frac{1}{\sqrt{\pi}\Delta\lambda_D} \exp\left[-\left(\Delta\lambda/\Delta\lambda_D\right)^2\right], \tag{2.19}$$

where

$$\Delta\lambda_D \equiv \frac{\lambda_0}{c}\sqrt{\frac{2k_\mathrm{B}T}{m}}\,, \tag{2.20}$$

is the Doppler width.

Another important broadening process stems from the finite lifetimes of the excited states in atoms. Heisenberg's uncertainty principle explains this broadening: a finite lifetime limits the accuracy of sharp atomic levels. This phenomenon is called *natural broadening* and gives the extinction profile a Lorentzian shape (similar to the Cauchy

distribution) with sharper a peak and wider wings than a Gaussian profile. The Lorentzian extinction profile per frequency looks like

$$\varphi(\nu - \nu_0) = \frac{(\gamma/4\pi)^2}{(\nu - \nu_0)^2 + (\gamma/4\pi)^2},$$

with the extinction coefficient per wavelength derived in Gray (2005, p. 234) as

$$\alpha_\lambda = \frac{e^2}{mc}\frac{\lambda^2}{c}\frac{\gamma\lambda^2/(4\pi c)}{(\lambda - \lambda_0)^2 + [\gamma\lambda^2/(4\pi c)]^2},$$

in CGS units.

In these equations, γ is the damping constant. This term comes from modelling an atom as a damped harmonic oscillator with a driving force (this is the photon). The damping term for natural broadening is denoted γ_{rad}.

The last microscopic broadening effect discussed here is collisional broadening. Collisional broadening comes from small-scale perturbations in the electric field caused by nearby particles. Such perturbations affect the energy levels of an atom through Coulomb interactions and consequently change the extinction or emission profile of said atom. Using the *impact approximation*, the broadening profile from collisional processes has a Lorentzian shape, just like natural broadening. The damping parameter of collisional broadening is called γ_{col}.

The total extinction profile is found by convoluting all the individual profiles. Considering the natural and collisional broadening, convolving the two Lorentz profiles simplifies to summing the damping parameters from the driven oscillators, $\gamma = \gamma_{\text{rad}} + \gamma_{\text{col}}$. In addition, we have to convolve the Gaussian profile stemming from thermal broadening to receive the total extinction profile. The result of this convolution produces the *Voigt* profile, given as

$$\varphi(\lambda - \lambda_0) = \frac{1}{\sqrt{\pi}\Delta\lambda_D} H(a, v), \tag{2.21}$$

with $H(a, v)$ the Voigt function. Following Rutten (2003, p. 59),

$$H(a, v) = \frac{a}{\pi}\int_{-\infty}^{+\infty} \frac{e^{-y^2}}{(v - y^2) + a^2}\,\mathrm{d}y, \tag{2.22}$$

where

$$v \equiv \frac{\lambda - \lambda_0}{\Delta\lambda_0},$$
$$a \equiv \frac{\lambda^2}{4\pi c}\frac{\gamma}{\Delta\lambda_D}.$$

2.4 Atomic populations

All processes that were described in the previous section are dependent on the population density of each energy level of atomic species in the atmosphere. In return, radiative processes alter the atomic populations: populations are coupled with the radiation field. Moving onward, the population density of an atomic species is denoted n_i for all discrete energy levels i the atom can assume.

2.4.1 Statistical equilibrium

When calculating the atomic populations, it is normal to assume a static situation where the atomic populations do not change with time. Atomic populations are determined solely from the atmospheric conditions present at any given time. Under this assumption, the rate of transitions away from level i is equal to the rate of transitions to the same level. The static assumption gives the equation

$$\sum_{j\neq i}^{N} n_j P_{ji} - n_i \sum_{j\neq i}^{N} P_{ij} = 0\,, \tag{2.23}$$

where P_{ij} is the probability for a transition between level i and j, given in units s^{-1}. When P_{ij} is multiplied with the number density of the atomic populations, we get the total rate of transitions per second per volume.

Because the rate P_{ij} includes both transitions from a lower to an upper level and transitions from an upper to a lower level, it is a conditional expression. Including all transitions mentioned in the previous sections, it is linked to the Einstein coefficients and the radiation field accordingly:

$$P_{ij} = \begin{cases} B_{ij}\bar{J}^{\varphi}_{\lambda_0} + C_{ij} & \text{if } i < j \\ A_{ij} + B_{ij}\bar{J}^{\chi}_{\lambda_0} + C_{ij} & \text{if } i > i \end{cases}\,. \tag{2.24}$$

2.4.2 LTE

In optically thick media (high mass density), the collisional rates are much higher than the radiative rates. Here, collisions dominate atomic transitions. Collisional rates depend solely on temperature and electron density, and consequently, the radiation field reflects the temperature in the media. This radiation is called thermal radiation and means that the "temperature" of radiation and the fluid are the same: the system is in LTE. In LTE, the source function is determined by temperature only and is equal to the Planck function: $S_\lambda = B_\lambda(T)$. The Planck function is given per wavelength as

$$B_\lambda(T) = \frac{2hc^2}{\lambda^5}\left[\exp\left(\frac{hc}{\lambda k_{\mathrm{B}} T}\right) - 1\right]^{-1}\,. \tag{2.25}$$

Under the assumption of LTE, it is also possible to derive an analytical expression for the atomic populations. The distribution of atomic levels on a given ionisation stage r

is found from the Boltzmann distribution. It describes the ratio of populations between two levels s and t as

$$\frac{n_{r,s}}{n_{r,t}} = \frac{g_{r,s}}{g_{r,t}} \exp\left(-\frac{\chi_{r,s} - \chi_{r,t}}{k_{\mathrm{B}}T}\right) , \tag{2.26}$$

where $\chi_{r,s}$ and $\chi_{r,t}$ are the energy levels measured from the ground level, respectively. The statistical weights $g_{r,s}$ and $g_{r,t}$ of level s and t counts the number of different electron configurations for the given level.

We also need the atoms' distribution over different ionisation stages to get the atomic populations. This distribution is also possible to derive in LTE and was done by the Indian physicist Meghnad Saha in 1920, whose name labels this distribution for different ionisation stages. The Saha distribution relates the populations of successive ionisation stages to each other. For the total population density of ionisation stages N_{r+1} and N_r, the distribution takes the form

$$\frac{N_{r+1}}{N_r} = \frac{1}{N_e}\frac{U_{r+1}}{U_r}\left(\frac{2\pi m_e k_{\mathrm{B}}T}{h^2}\right)^{3/2} \exp\left(-\frac{\chi_r}{k_{\mathrm{B}}T}\right) . \tag{2.27}$$

Here N_e is the electron density, and χ_r is the ionisation energy for stage r. The partition function U_r for a stage r is calculated as a weighted sum over the statistical weights, specifically

$$U_r \equiv \sum_s g_{r,s} \exp\left(-\frac{\chi_{r,s}}{k_{\mathrm{B}}T}\right) .$$

The combination of the Boltzmann and Saha Equations (2.26) and (2.27) produces a distribution that describes the ratio between the populations of a stage i and an ionisation state c that the atom ionises to. This distribution combines both in name, to the Saha-Boltzmann distribution, and mathematically, to

$$\frac{n_c}{n_i} = \frac{1}{N_e}\frac{2g_c}{g_i}\left(\frac{2\pi m_e k_{\mathrm{B}}T}{h^2}\right)^{3/2} \exp\left(-\frac{\chi_{ci}}{k_{\mathrm{B}}T}\right) . \tag{2.28}$$

Here, χ_{ci} is the energy difference between level i and ion state c, i.e.

$$\chi_{ci} = \chi_r - \chi_{r,i} + \chi_{r+1,c} .$$

2.5 Voronoi diagram

The Voronoi diagram is used to calculate radiative transfer throughout this work. This section presents a quick overview of the diagram's definition and a recipe explaining how to sample points from which I construct the Voronoi diagram.

2.5.1 Definiton

A Voronoi diagram is calculated from a set of control points, also called sites. These sites are the counterpart to the grid points in radiative transfer calculations on a regular grid. Every quantity regarding radiative transfer is defined at these sites.

The Voronoi Diagram is characterised by the set of Voronoi cells spanned by the control points. Studied as early as 1644 by Rene Descartes, the Voronoi Diagram was defined for 2 and 3 dimensions by Peter Gustav Lejeune (Dirichlet, 1850), and generalised to n dimensions by Georgy Voronoi (Voronoi, 1908).

A formal definition can be phrased as follows: *Let X be a metric space with distance function d. Let $\{\vec{p}_i\}_{i=1,\dots,n}$ be the sites in the space X. The Voronoi cell, or Voronoi region, R_k, associated with the site $\vec{p}_k$ is the set of all points in X who are closer to p_k than every other site $\vec{p}_j$ in X, where $j \neq k$.*

In simpler terms, the Voronoi cell associated with a control point is defined as every point closer to that control point than to every other control point.

To calculate the Voronoi cell, we insert planes between a control point and the other sites in the grid. Neighbouring points are found by eliminating planes. The boundary between two neighbouring control points is a plane extending from the mid-point of the vector between the control points. This plane has to be perpendicular to the vector between the control points.

Lines between the control points are referred to as the Delaunay lines, after mathematician Boris Delaunay for his work on the Delaunay triangulation (Delaunay, 1934). For radiative transfer calculations, rays can be propagated along these lines, following the work of e.g. the SIMPLEX2 (Paardekooper et al., 2010) or LIME (Brinch & Hogerheijde, 2010) radiative transfer codes.

2.5.2 Sampling an irregular grid for radiative transfer

To obtain a grid better suited for radiative transfer, more points should be placed in regions where the radiation field sustains large variations. To emphasise these regions, we need a sampling method that gives a higher density of control points at these locations—but we cannot neglect the rest of the atmosphere. In my work, I have used a Monte Carlo based technique to construct the control points for the radiative transfer simulation, namely rejection sampling.

Rejection sampling uses a reference distribution to draw points. The reference distribution acts as a probability distribution, determining how likely it is to find a control point in a given area. The benefit of rejection sampling is that the reference distribution can assume any form, as long as it is finite—the reference distribution does not have to follow any of the well-known probability density functions.

The rejection sampling method is advantageous in the following situation. Assume we have a *target distribution* $f(\vec{x})$ from which we want to sample control points and

a *proposal distribution* $g(\vec{x})$ from which we can easily sample random numbers. The function $f(\vec{x})$ can, for example, take the shape of the neutral hydrogen density in the solar atmosphere, while the proposal distribution can be the uniform distribution U. Because the hydrogen density does not look like a standard probability function—it is also impossible to invert—we can use rejection sampling to generate samples (sites). This method works as follows:

1. A proposal position $\vec{x}_{\text{proposal}}$ is drawn from the proposal distribution, and gives the proposal density $p_{\text{proposal}} = f(\vec{x}_{\text{proposal}})$.
2. A random rejection density $p_{\text{rejection}}$, is drawn from the uniform distribution U.
3. The proposal density is compared with the rejection density. If $p_{\text{proposal}} \geq p_{\text{rejection}}$, then the proposal position is accepted as a control point. Else, the proposal position is rejected, and the method is repeated.
4. Go back to 1. until the required number of samples are drawn.

Chapter 3

Methods

3.1 Code

The code used for calculations in this work was developed in the programming language `Julia` (Bezanson et al., 2017), using its native *thread parallelism* to speed up computations. All source code related to this project is open source and available on GitHub (Udnæs, 2022).

3.2 Model atmosphere

A solar atmospheric model has traditionally been a semi-empirical model. The semi-empirical model is derived under certain assumptions, e.g. a plane parallel atmosphere or a hydrostatic equilibrium. The above assumptions are used in the well-known FALC model, a one-dimensional solar atmosphere derived by Fontenla et al. (1993). While these models helped progress the understanding of radiative transfer, they lack realistic details present in the solar atmosphere. An example is the three-dimensional velocity field that accounts for important processes in spectral line formation, such as macroscopic Doppler shifting.

The later years' evolution of computers has realised three-dimensional magnetohydrodynamic (MHD) simulations, capable of describing more complex and realistic structures in the solar atmosphere. In my work, I solve the RTE in a three-dimensional model atmosphere produced by the stellar atmosphere code *Bifrost* (Gudiksen et al., 2011).

The model in question is a quiet Sun simulation. It is a snapshot with $256 \times 256 \times 430$ grid points, extending 6.0 Mm in both horizontal directions of the plane, and 8.7 Mm in the vertical direction. The horizontal resolution is constant at $23.4\,\mathrm{km} \times 23.4\,\mathrm{km}$ per pixel, while the vertical resolution varies slightly through the atmosphere: it is finer at the bottom of the model, and a little coarser at the top. The mean vertical resolution

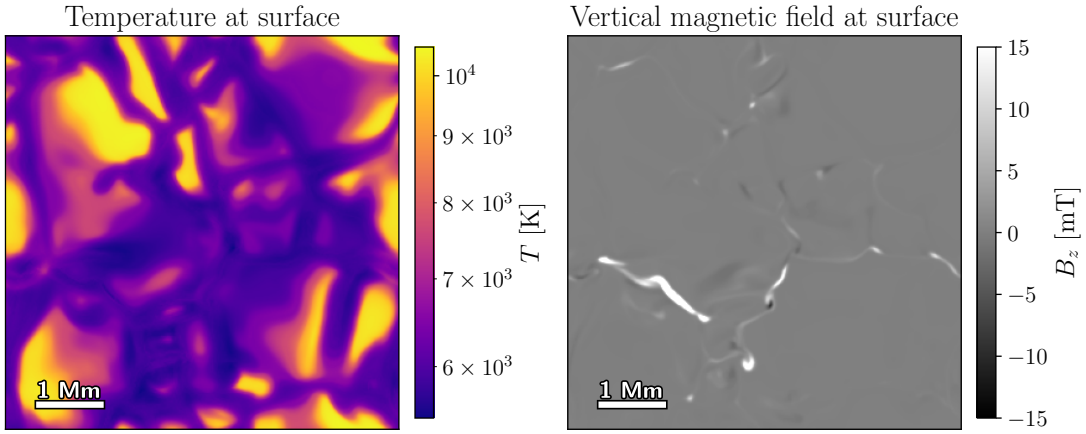

Figure 3.1: Temperature and z-component of the magnetic field in the model atmosphere. These data are taken at vertical location $z = 6.8$ km—the surface in the model.

is 20.3 km. Each point holds information for magnetic field (B_x, B_y, B_z), hydrogen density N_H, electron density N_e, temperature T, and velocity field (v_x, v_y, v_z). All these quantities are used for this thesis's radiative transfer calculations, except the magnetic field, which is not needed for unpolarised radiative transfer.

Since the model is meant to reproduce the quiet Sun, there is little activity on the surface. The mean unsigned magnetic field at the surface is 0.50 mT. Figure 3.1 displays physical conditions at the surface in terms of temperature and vertical magnetic field. The temperature image shows features from granules on the surface. The magnetic field image shows little activity except for a magnetic brightening near the lower left corner of the image.

3.2.1 Boundary conditions

The method of characteristics always starts at either the upper or lower boundary of a given problem. Therefore it is necessary to fix these boundaries.

At the bottom boundary of the solar atmosphere, the density is thick, and the radiation is assumed to be thermalised.[1] I use the Planck function to determine the lower boundary.

At the upper boundary, the mass density is very low. We imagine this region to border empty space. Therefore, a reasonable upper boundary condition is to set the incoming radiation to zero.

[1] Collisions between atoms and other particles dominate atomic transitions in optically thick media. Collisions come from microscopic motions in the media that are determined by temperature. Consequently, the radiation field follows temperature, which is LTE described in Section 2.4.2.

3.3 Constructing an irregular grid

An irregular grid is the most general grid we can work with. The only condition I impose is constraining the grid points to lie within the borders of the original atmospheric parameters. It follows that for a site $\vec{p_i} = (x_i, y_i, z_i)$, these demands must be fulfilled:

$$\begin{aligned} x_i &\in [x_{\min}, x_{\max}] \ , \\ y_i &\in [y_{\min}, y_{\max}] \ , \\ z_i &\in [z_{\min}, z_{\max}] \ . \end{aligned}$$

With just this restriction on where grid points can lie, it is impossible to assume any structure in the grid. Therefore, we cannot exploit properties of the grid to make calculations efficient.

By making the grid better suited to perform radiative transfer calculations, we can justify the drawback in efficiency an irregular grid brings. Thus, we can sacrifice performance for better results. One approach to optimise the grid for radiative transfer is to sample the grid such that the density of grid points follow the extinction coefficient α_λ. This approach is analogous to minimising the difference in optical depth between grid points (as done in 1D by Carlsson, 1986, see Section 2.2), because the extinction coefficient acts as a probability density for optical depth τ.[2] Sampling grid points from such a distribution is not straightforward. The extinction coefficient will certainly not look like one of the standard empirical probability distributions. Therefore, I obtain the grid points with a Monte Carlo technique. This method is called rejection sampling, and is already described in Section 2.5.2. Although the extinction coefficient is not the only quantity I sample grids points from, I always use the rejection sampling technique.

In radiative transfer, we need nearby locations to simulate the radiation field, e.g. calculating the formal solution. Due to this fact, we need information on grid points in the vicinity of each other. To fulfil this demand, I construct a Voronoi diagram of the entire grid and store information about the neighbours associated with each grid point. An example of such a Voronoi diagram is presented in Figure 3.2.

The Voronoi diagram is calculated with the open-source library `voro++` (Rycroft, 2009). The only statistics from the Voronoi diagram that is relevant for the RT simulation, is a list of neighbours for every site in the irregular grid. For efficient calculations, the lists of neighbours are stored in a matrix. In this matrix, every grid point corresponds to a row. The first column in this matrix tells how many neighbours N_i a site i has, and the next N_i entries hold the indices of the neighbours. The number of columns in the matrix is $\max(N_i) + 1$ (meaning that several rows in the matrix contain some "empty" entries).

[2] Optical depth can be thought of as the unnormalised cumulative distributive function of α_λ. It is indeed calculated as an integral of the extinction coefficient over the entire domain. The extinction coefficient is an exclusively positive value, fulfilling an important demand of a probability density function.

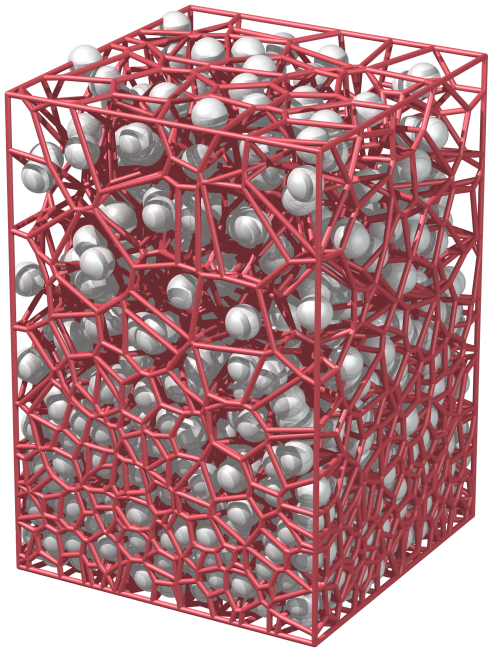

Figure 3.2: Example Voronoi grid adapted from a *Bifrost* atmospheric model and downsampled to fewer points to clarify the features of the grid. This particular grid is constructed by sampling grid points according to hydrogen density. In the figure, white points represent sites, and red lines indicate the edges between cell borders in the Voronoi diagram.

I propagate intensity in the ray direction, similar to the LC and SC methods. Radiation is calculated layer by layer through the domain, making it necessary to keep track of the layers in the grid. Layer order is not the same when we work our way downwards from the top to the bottom of the atmosphere or upwards from the bottom to the top. Therefore, two arrays are required to store information of layers: one for rays propagating upwards and one for rays propagating downwards. I calculate the layers of the grid in the following manner:

if Characteristic rays move upwards **then**
    Find all grid points that neighbour the bottom border of grid, assign to layer 1
    Find all grid points that neighbour layer 1, assign to layer 2
    Continue until all sites are placed in a layer
else if Characteristic rays move downwards **then**
    Find all grid points that neighbour the top border of grid, assign to layer 1
    Find all grid points that neighbour layer 1, assign to layer 2
    Continue until all sites are placed in a layer
end if

Figure 3.3 illustrates the layers for a grid drawn from a uniform distribution with 21^3 sites. Here, we can see sites marked by layer. The layering is different for the two cases where radiation moves upwards or downwards through the domain.

3.3.1 Interpolating from a regular to a Voronoi grid

In general, sites will not be sampled at locations where physical quantities were previously defined. Having knowledge of the atmospheric parameters from the regular grid

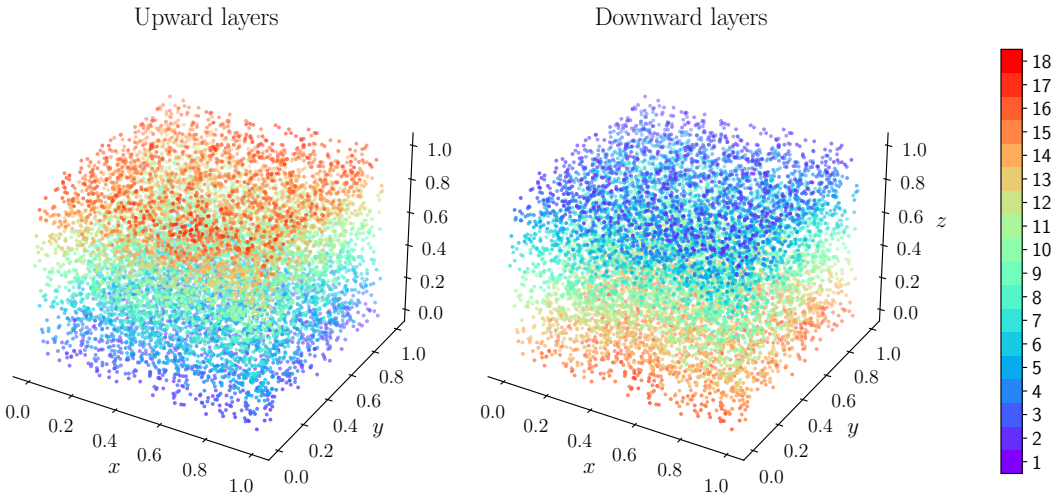

Figure 3.3: Example grid constructed by drawing sites from a uniform distribution. This grid—which is a $1 \times 1 \times 1$ box in dimensionless units with 21^3 Voronoi sites—has no intrinsic physical meaning, and is only meant to conceptualise the algorithm. In the plots, we see colour graded layers sorted from the bottom and up (left plot), or from the top and down (right plot). The ray tracing algorithm starts at one of the boundaries, and works it way sequentially through the layers.

makes it possible to estimate values on the new sites through interpolation.

One simple interpolation method is linear interpolation, dubbed *trilinear* interpolation in three dimensions. Trilinear interpolation uses two points per axis, similar to linear interpolation in one dimension. With three axes, we need eight values for one estimate. The points used to interpolate to a new site are the eight grid points closest to the new site. These eight grid points are the corners of the box enclosing the site.

The interpolation is performed as follows. First, find the relative difference between the interpolation points and the site in each direction:

$$x_d = \frac{x - x_0}{x_1 - x_0}\,,$$
$$y_d = \frac{y - y_0}{y_1 - y_0}\,,$$
$$z_d = \frac{z - z_0}{z_1 - z_0}\,.$$

Then, we interpolate in the x direction accordingly:

$$c_{00} = c_{000}(1 - x_d) + c_{100}x_d\,,$$
$$c_{01} = c_{001}(1 - x_d) + c_{101}x_d\,,$$
$$c_{10} = c_{010}(1 - x_d) + c_{110}x_d\,,$$
$$c_{11} = c_{011}(1 - x_d) + c_{111}x_d\,.$$

Having interpolated in the x direction, we interpolate along y, giving

$$c_0 = c_{00}(1 - y_d) + c_{10}y_d\,,$$
$$c_1 = c_{01}(1 - y_d) + c_{11}y_d\,.$$

Finally, we get the estimate c by "pushing" along the z-axis,

$$c = c_0(1 - z_d) + c_1 z_d\,. \tag{3.1}$$

The choice of linear interpolation can negatively impact the accuracy of the result. Linear interpolation is a weighted average of the interpolation points, effectively smoothing the interpolated quantities. Thus, the linear method will never introduce new maxima or minima. Lacking the ability to yield new extreme values can also be a strength of the linear method. Due to its simplicity, it is not subject to oscillations or over-fitting, to which higher-order methods are prone.

3.3.2 Interpolating back to a regular grid

After the radiative transfer simulation with the Voronoi grid is finished, it is beneficial to convert all atmospheric variables—including source function and level populations—back to a regular grid. Model atmospheres with a corona, such as the *Bifrost* atmosphere used in this thesis, will often give irregular grids with a coarse resolution at the top of the atmosphere (if the grid is sampled to reflect mass density or continuum extinction). A coarse resolution in the top layers loses spatial resolution when calculating outgoing intensity. Therefore, I interpolate the atmospheric variables from the irregular grid back to a Cartesian grid with the original domain boundaries. This grid can have a higher resolution (i.e. more grid points) than the irregular grid to ensure that variations from regions with a high density of sites in the irregular grid are captured onto the regular grid. I use the irregular grid to converge the source function and populations better; I interpolate back to a regular grid for accurate calculations of outgoing intensity.

Interpolation on an irregular grid is more challenging than interpolation on a regular grid because the irregular grid lacks regularity. The nearest neighbour interpolation is the simplest interpolation method. This interpolation method sets a point's value equal to the value at the nearest site. Given that the irregular grid is constructed as a Voronoi tessellation, this is the same as saying that quantities are constant within the Voronoi cell.

Another simple method of interpolation on an irregular grid is the *inverse distance interpolation*, also known as *inverse distance weighting*. This method gives the interpolant as a weighted sum of the k nearest sites where the weights are given as the inverse distance to the respective sites. The interpolant is calculated as

$$u(\vec{x}) = \frac{\sum_{i=1}^{k} \omega_i(\vec{x}) u_i}{\sum_{i=1}^{k} \omega_i(\vec{x})}\,, \tag{3.2}$$

where u_i are the quantities at a site, and the weights

$$\omega_i(\vec{x}) = \frac{1}{d(\vec{x}, \vec{x})^p}$$

are the inverse distances to the power of p. For $p \to \infty$ or $k = 1$, this method reduces to the nearest neighbour interpolation.

3.4 Ray tracing

Before the radiative transfer simulation on irregular grids was developed, I created a 3D short characteristics framework. This framework is used to compare radiative transfer methods on irregular grids with the standard methods.

Both the irregular and regular grid methods have common ground. The formal solution is calculated in the same manner, meaning that I apply the same approximation of the continuous integral in Equation (2.7). In this work, the formal solution is approximated by piecewise linear integration. Only needing two values for the source function, this approach makes the intensity along each characteristic quick to compute.

The naive nature of piecewise linear integration can result in decreased accuracy of the solution. Higher-order methods can be used to improve accuracy, but most of these methods are not reliable in the presence of discontinuities or even in high gradient regions (as discussed in Janett, 2019). Due to oscillations, they can be prone to spurious solutions and may even introduce negative solutions in the source function. Nevertheless, higher-order methods that tolerate sharp gradients or discontinuities do exist. In particular, there are higher-order methods of the Diagonal Element Lambda Operator family (proposed by Rees et al., 1989, abbreviated DELO) able to handle sharp gradients. For polarised radiative transfer, the DELO-Bezier interpolants presented in de la Cruz Rodríguez & Piskunov (2013) improved the DELO's ability to handle sharp gradients. A new concept dealing with discontinuities, as opposed to the DELO methods, was presented in Steiner et al. (2016). In the paper, "piecewise continuous reconstruction and slope limiters is applied to the source function" to solve the polarised RTE. This evolution of higher-order methods has seen better convergence on simplified atmospheric models. However, Janett et al. (2018) suggests that "the high intermittency of 3D R-MHD models might thwart high-order convergence even in fine numerical grids" and higher order DELO methods. For simplicity and the purposes of this thesis, the simple linear approach is justifiable. In the following paragraph, I outline a more detailed description of the numerical formal solution with the piecewise linear approach.

3.4.1 Linear interpolation of the formal solution

On the discretised grid, the source function S_λ and extinction coefficient α_λ are only known in the cell centres, making it necessary to interpolate these quantities to calculate

the formal solution. If we use the cell centre i and the upwind position of the ray $i-1$ to approximate the integral from Equation (2.7), the formal solution takes the form

$$I_i = \exp\left(-\Delta\tau_{i-1}\right) I_{i-1} + a_i S_{i-1} + b_i S_i \,. \tag{3.3}$$

The linear coefficients in this equation are given by

$$a_i = \left[1 - \exp\left(-\Delta\tau_{i-1}\right)\right] / \Delta\tau_{i-1} - \exp\left(-\Delta\tau_{i-1}\right), \tag{3.4}$$

$$b_i = 1 - a_i - \exp\left(-\Delta\tau_{i-1}\right). \tag{3.5}$$

In the limit $\Delta\tau \to 0$, the calculations of the linear weights in Equations (3.4) and (3.5) fail on computers due to the finite accuracy of floating-point numbers. Double precision floating point numbers produce noticeable errors in the calculation of the coefficients already at $\Delta\tau \sim 10^{-14}$, and at smaller optical depths, the error becomes adverse.

A Taylor expansion of the coefficients around $\Delta\tau = 0$ fixes the lower limit of optical depth. Including second order terms in the expansion, the negative exponential is

$$\exp\left(-\Delta\tau_{i-1}\right) = 1 - \Delta\tau_{i-1} + \frac{1}{2}\Delta\tau_{i-1}^2 \,,$$

and the coefficients become

$$a_i = \frac{1}{2}\Delta\tau_{i-1} - \frac{1}{3}\Delta\tau_{i-1}^2 \,,$$

$$b_i = \frac{1}{2}\Delta\tau_{i-1} - \frac{1}{6}\Delta\tau_{i-1}^2 \,,$$

when $\Delta\tau_{i-1} \ll 1$. Expanding the coefficients ensures that the limit of the expressions are correct,

$$\lim_{\Delta\tau\to 0} a_i = \lim_{\Delta\tau\to 0} b_i = 0 \,,$$

even with computer arithmetic. Since the medium does not add radiation to the beam when the optical depth goes to zero, this is the intuitive value of the coefficients in the lower limit.

It is also possible to approximate the coefficients in the high limit $\Delta\tau_{i-1} \gg 1$, because the term $\exp\left(-\Delta\tau_{i-1}\right)$ vanishes quickly at high optical depths. Expanding the coefficients in this region is not done to improve the accuracy of the result but rather to avoid evaluating the costly exponential functions in Equations (3.4) and (3.5). The negative exponential is approximated as

$$\exp\left(\Delta\tau_{i-1}\right) = 0$$

in this limit, and the coefficients become

$$a_i = 1/\Delta\tau_{i-1} \,,$$

$$b_i = 1 - a_i \,.$$

Using a linear interpolation of the extinction coefficient makes a very simple expression for the optical depth increment $\Delta\tau_{i-1}$. The resulting integral in Equation (2.3) is easily solved with the trapezoidal rule as

$$\Delta\tau_{i-1} = \frac{1}{2}\Delta z_{i-1}\left(\alpha_i - \alpha_{i-1}\right) . \tag{3.6}$$

3.4.2 Tracing rays through a regular grid

I use a linear interpolation of the source function for the short characteristics method. With a linear interpolation, the formal solution is calculated by Equation (3.3). We need two spatial points to perform this calculation. One of the points is the grid point i where we wish to find the intensity I_i, while the other point $i-1$ is the upwind position. This position is dependent on the ray's direction and is found by tracing the ray from the grid point i and backwards until the ray intersects one of the planes extended by the computational grid. The upwind point exists on one of the faces of the voxel spanned by the neighbouring grid points. The face where the upwind point resides is determined by the ray's direction and the grid's spacing. Because the upwind point is located between grid points, interpolation is required. I interpolate the following quantities at the upwind location: extinction coefficient, source function, and intensity. These values are found through bilinear interpolation.

If the upwind point lies on one of the faces extending vertically, the incident intensity I_0 in Equation (2.7) is not straightforward to compute. Only incident intensities at layers below the ray are known in the method of characteristics. At the beginning of a sweep, the intensities at the current layer are unknown, and it is impossible to interpolate the value of I_0 using the same current layer. I_0 can be found by extending the ray until it reaches the below layer (as done in e.g. Hayek et al., 2010; de Vicente et al., 2021). Another method I found easier to implement is to start by assuming all intensities at the current layer to be zero. Although it is not accurately computed in the beginning, the upwind intensity can be interpolated from the current and lower layers. As the current layer is swept through, grid points are populated with non-zero intensities. When the entire layer is calculated, the process is repeated with the updated intensities, this time getting more accurate values for I_0. Several passes can be performed for each layer, in principle saturating the layer with every sweep. Passes are repeated until incident intensities obtain desired accuracy. This method is easy to implement and requires immediate neighbours of a current grid point only, as opposed to extending the ray across several cells to find the upwind intensity. I found that the layers saturated after three passes, effectively finding the correct solution.

An advantage of the short characteristics method is that one sweep through the entire domain calculates intensities for every grid point. After a sweep is performed, the contribution to the mean intensity J_λ is added with Equation (2.11).

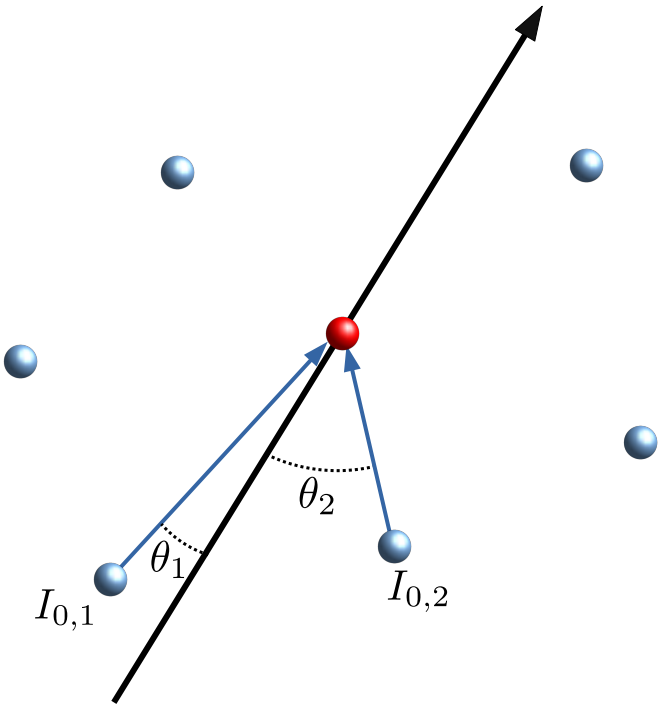

Figure 3.4: Two-dimensional representation of ray tracing in an irregular grid. The red point is the site where radiation is calculated, and the thick black ray is the direction of the ray. The incoming radiation comes from the sites with the smallest angles between the Delaunay lines and the direction of the beam. These angles are marked in the figure as θ_1 and θ_2. The incoming radiation comes from the two sites spanning these angles, giving $I_{0,1}$ and $I_{0,2}$ as incident intensities.

3.4.3 Tracing rays through a Voronoi grid

Ray tracing through the irregular grid is inspired by the short characteristics method, and the radiative transfer codes LIME (Brinch & Hogerheijde, 2010) and Simplex2 (Paardekooper et al., 2010). The similarity with the LIME and Simplex2 codes is tracing rays along the Delaunay lines in the Voronoi tessellation. Similarly to the SC method, I calculate intensity layer by layer with a piecewise linear interpolation of the source function. The upwind intensity is found from the immediate layer below. Then, the formal solution is solved with a linear approximation of the source function, per Equation (3.3). Since intensity is calculated layer by layer, the computational complexity of this method scales as $\mathcal{O}(n_{\text{sites}})$, equivalent to SC's $\mathcal{O}(N^3)$ cost.

A sketch of the Delaunay ray tracing method is shown in Figure 3.4. The incoming ray to a site is split into two parts, and the formal solution is calculated as a weighted sum of rays along two Delaunay lines. These two Delaunay lines are the ones with the orientation that make the smallest angles with the direction of the ray under consideration. By weighting the formal solution over two rays, I mitigate some of the error originating from the difference in direction between the Delaunay lines and the direction of the ray.

The formal solution that is calculated along the two Delaunay lines is weighted by the dot product between the Delaunay lines and the ray's direction. This weighting emphasises the Delaunay line closest to the ray. When computing the dot product, the ray's direction is normalised to the unit vector $\vec{k}$, and the orientations of the Delaunay lines are denoted $\vec{D}_j$. For a site $\vec{p}_i$ and its neighbours $\vec{p}_j$, the Delaunay lines' orientations

are calculated as

$$\vec{D}_j = \frac{\vec{p}_i - \vec{p}_j}{\|\vec{p}_i - \vec{p}_j\|} \,.$$

The dot product between the ray and the Delaunay lines are then found by

$$v_j = \vec{k} \cdot \vec{D}_j \,.$$

To clarify, the Delaunay lines that are used to calculate intensity are the two lines spanning the smallest angle from the ray. These are also the lines giving the two largest dot products, called v_{k_1} and v_{k_2}. These products are expected to be close to one.[3] Intensity at the cell centre is calculated as a weighted sum of the formal solution over these two Delaunay lines. With the linear interpolation of the formal solution, Equation (3.3) is transformed into

$$I_i = \sum_{j=k_1,k_2} \left[\exp\left(-\tau_j\right) I_j + a_j S_j + b_j S_i\right] w_j \,, \tag{3.7}$$

where w_j are the weights for the Delaunay lines that produce the smallest angle with the ray (k_1 and k_2). The weights have to be normalised, and favour a smaller angle—or a larger dot product. Therefore, they are calculated as

$$w_j = v_j^r \Bigg/ \sum_{j=k_1,k_2} v_j^r \,. \tag{3.8}$$

The parameter r is introduced to give more weight to the neighbour closest to the ray, thus $r > 1$. A suitable value was found experimentally as $r = 7$; however, further experimentation with this value is needed.

In Equation (3.7), the linear coefficients for the formal solution are calculated from the site $\vec{p}_i$ and the neighbours $\vec{p}_{k_1}$ and $\vec{p}_{k_2}$. These are locations where values for the extinction coefficient, source function, and upwind intensity were previously defined. Therefore, there is no requirement for interpolation to get the upwind values with the Delaunay ray tracing method.

The weighting method to calculate incident intensity is different from the LIME (Brinch & Hogerheijde, 2010) or the Simplex2 (Paardekooper et al., 2010) RT codes. These codes use a Monte Carlo walk to trace rays through the grid. When I tried the same random method to trace rays, the grid was traversed differently in every Λ-iteration. The randomness of this traversing introduced some noise to the mean intensity. This, in turn, hampered convergence of the Λ- iterations. In principle, a solution could be to use the same random seed for every iteration, making the radiation travel a consistent path for every iteration; however, this would introduce bias to the method. Through

[3] In an irregular grid with sites drawn from a 3D Poisson distribution, a site has on average 15.54 neighbours (van de Weygaert, 1994). With ∼ 300 000 sites drawn according to the hydrogen density, the average number of neighbours was 15.44. Consequently, every site should have some neighbours whose Delaunay line only differs by a small angle from the characteristic ray.

the dependence on the random seed, the point of using the Monte Carlo method would disappear. Therefore, I used the weighting method.

Similarly to the SC method, the Delaunay ray tracing method performs multiple passes through each layer. When the rays are shallow, there is a big chance that the Delaunay lines we trace downwards are in the same layer as the current site. In this layer, all sites are initialised with zero radiation. Consequently, information will be lost if the incident intensity stems from the same layer. With multiple passes through a layer, intensity saturates a layer similarly to the SC method. I found that three passes saturated the layers. Thus, information is recovered for shallow rays, yielding a correct propagation through the medium.

3.5 The two-level atom

To test the implementation of the irregular grid, I constructed a two-level atom model, using elements of code developed by Ida Hansen in her master thesis (Hansen, 2021) and functions from the `Julia` package `Transparency.jl` (Pereira, 2021).

The two-level atom simplifies the hydrogen atom, but there are significant differences from the physical atom. Similarly to the real hydrogen atom, the model has one proton in the nucleus and one orbiting electron; however, the model electron can only assume two energy levels—a ground state and a first excited state. It is also possible for the electron to be ionised, technically making it a 2+1 level model: two bound-bound states plus continuum. Another major difference from the real hydrogen atom is artificially increased collision rates to decrease the amount of scattering. The reasoning behind this modification is explained later in Section 3.5.1. Nonetheless, the same artificially increased collision rates are used for calculations on both grids, enabling comparison between the regular and irregular grids' results.

Following atomic data based on a real hydrogen atom, I construct the atomic model according to Table 3.1. The atom's energy levels give the spectral line corresponding to Lyman-alpha (Ly-α), but the line is not realistic because the model is simplified and has artificially increased collision rates.

For the two-level atom model, I assume *complete redistribution* (CRD). This means that the extinction profile and emission profile are identical:

$$\varphi(\lambda - \lambda_0) = \chi(\lambda - \lambda_0)\,. \tag{3.9}$$

CRD is valid when all deexcitation processes from u to l are independent of the exciting processes that put the atom in state u. In reality, this assumption is not valid for the Ly-α line, but the assumption is kept to keep the coding simple. The Voigt profile gives the line profile for the two-level atom in Equation (2.21). The monochromatic line extinction coefficient in CRD is expressed per wavelength as

$$\alpha_\lambda^l = \frac{hc_0}{4\pi\lambda_0}\varphi(\lambda - \lambda_0)\left[n_i B_{ij} - n_j B_{ji}\right]\,. \tag{3.10}$$

Table 3.1: Atomic data for the two-level atom. First column shows energy of the level given in cm^{-1}, second column is the statistical weight g for each level, and third column labels the electron configuration. Data obtained from NIST (Kramida et al., 2021).

$E\ [\mathrm{cm}^{-1}]$	g	label
0.000	2	H I 1S 2SE
82,258.211	8	H I 2P 2PO
109,677.617	1	H II continuum

Because the model atmosphere has a three-dimensional velocity field, there are macroscopic Doppler shifts of the line profile in every location of the atmosphere. The Doppler shifts are produced by the line of sight velocity v_{los} of the fluid with respect to a beam with direction $\vec{k}$. The line of sight velocity is calculated as the dot product between the direction vector $\vec{k}$ of the beam and the velocity $\vec{v}$ of the fluid. If λ_0 is the line centre in the rest frame and λ_0' is the line centre in the observer's frame, then the resulting shift of the line centre in the observer's frame is

$$\lambda_0' = \lambda_0 \left(1 + \frac{v_{\mathrm{los}}}{c}\right) . \tag{3.11}$$

To obtain the total extinction coefficient, I sum the line extinction with the continuum extinction. The continuum extinction is split into absorption processes and scattering processes, where absorption extinction comprises:

- Free-free extinction from the H^- ion calculated with the recipe from Stilley & Callaway (1970).
- Bound-free extinction from H^- found by Geltman (1962).
- Free-free extinction for hydrogen following Mihalas (1978, p. 101) and Rutten (2019, p. 68).
- Free-free extinction from H II$^+$ according to the recipe from, Bates (1952).
- Bound-free extinction from H II$^+$ molecules also with Bates (1952).

The scattering processes contributing to the extinction are Thomson scattering from Equation 2.18 and Rayleigh scattering following Dalgarno (1962). The continuum extinction varies marginally over the line wavelengths. Therefore, the continuum extinction is calculated only at the line centre of the rest frame. The total extinction coefficient becomes

$$\alpha_\lambda = \alpha_\lambda^l + \alpha_{\lambda_0}^c . \tag{3.12}$$

After calculating the extinction coefficient, we can compute the radiation field. The radiation field is found on the regular grid by the short characteristics method or the irregular grid with the Delaunay ray tracing method. We need an appropriate quadrature to compute the mean intensity. Popular choices of quadratures are the ones defined in *Methods in Computational Physics* (Carlson, 1963); however, more recent studies on quadratures are more suited for 3D. These are given in the series of papers by Štěpán et al. (2020) and Jaume Bestard et al. (2021), which will be used in this work. In particular, I use their twelve ray quadrature for unpolarised radiative transfer. The quadrature gives the angles and weights for each ray, from where the radiation field is found by Equation (2.11).

Calculating the mean radiation field is the first step of a Λ-iteration. The next step I do is updating the source function with Equation (2.14). This equation also holds for the two-level atom. However, the photon destruction probability ε_λ must be calculated to find the source function. This quantity is found as the absorption extinction divided by the total extinction. From Rutten (2003, p. 68), we can see that the photon destruction probability can be coined in terms of the collisional and natural rates—

$$\varepsilon_\lambda = \frac{C_{21}}{C_{21} + A_{21} + B_{21}B_{\lambda_0}} \tag{3.13}$$

—that is the same over the entire line ($\varepsilon_\lambda = \varepsilon$).

The mean intensity field is not only used to calculate the source function—but also provides information to calculate the atomic populations. To calculate the populations, I need both the radiative and collisional rates. The collisional rates are purely temperature dependent and calculated once only; however, the radiative rates have to be calculated in every iteration due to their dependence on the mean radiation field. The total rate for every transition within the two-level atom is then found by summing radiative and collisional rates.

Calculations must be performed for an appropriate number of wavelength points for every atomic transition to get accurate results. For the bound-bound transition, I sample the wavelength grid logarithmically (similar to Uitenbroek, 2001; Hansen, 2021). This grid is symmetric around the line centre, with a higher density of points in the core and a lower density in the wings. For the bound-free transitions, I sample the wavelength grid linearly. The points are sampled from the ionisation edge $\lambda_{\mathrm{max},1}$ to the minimum wavelength defined by $\lambda_{\mathrm{min},1} = \lambda_{\mathrm{max},n}\,(n/2)^2$ (Hansen, 2021). Here, $\lambda_{\mathrm{max},1}$ is the ionisation wavelength edge from the ground level, and n is the level number.

Now, we have everything needed to solve the statistical equilibrium Equation (2.23), subsequently finding the atomic populations. The statistical equilibrium equation gives us $n_{\mathrm{levels}} + 1 = 3$ equations with the same number of unknown populations. Because the total hydrogen density $n_{\mathrm{tot}} = N_H$ is known from the model atmosphere, we can

constraint the solution by

$$\sum_{i=1}^{N} n_i = n_{\text{tot}} \Rightarrow n_1 = n_{\text{tot}} - \sum_{i=2}^{N} n_i \,.$$

Substituting the ground level population with the above expression, the populations are obtained through the following steps:

$$\begin{aligned}
n_i \sum_{j\neq i}^{N} P_{ij} - \left(n_{\text{tot}} - \sum_{j\neq 1}^{N} \right) P_{1i} - \sum_{j\neq i,1}^{N} n_j P_{ji} &= 0 \,, \\
n_i \sum_{j\neq i}^{N} P_{ij} + \sum_{j\neq i,1}^{N} n_j P_{1i} + n_i P_{1i} - \sum_{j\neq i,1}^{N} n_j P_{ji} &= n_{\text{tot}} P_{1i} \,, \\
n_i \left(P_{1i} + \sum_{j\neq i}^{N} P_{ij} \right) + \sum_{j\neq i,1}^{N} n_j \left(P_{1i} - P_{ji} \right) &= n_{\text{tot}} P_{1i} \,,
\end{aligned}$$

where we end up with a solution that can be recognised as a matrix equation. The populations are written as a vector $\vec{n}$ solved as $\vec{n} = A^{-1}\vec{b}$. For this equation to hold, then the matrix $A = (a_{ij}) \in \mathbb{R}^{(N-1)\times(N-1)}$ is on the form

$$\begin{aligned}
a_{ij} &= P_{1i} + \sum_{j\neq i}^{N} P_{ij} && \text{for } i = j \,, \\
a_{ij} &= P_{1i} - P_{ji} && \text{for } i \neq j \,,
\end{aligned}$$

and the vector $\vec{b}$ has the elements

$$b_j = n_{\text{tot}} P_{1i} \,.$$

Calculating populations is the last step in one single iteration. After the populations are calculated, I write intermediate results to file. Then I check for convergence or go on to the next iteration.

3.5.1 Convergence

The Λ-iterations are performed until the solution converges. In this context, convergence is understood as a stabilisation of the source function. For every wavelength, I calculate the relative change of the source function in two subsequent iterations. An indicator for convergence is the maximal absolute value of this relative change. I demand the indicative value to be smaller than the convergence criterion ϵ, per Equation (2.17). When this criterion is met, the solution is said to converge. In this work, I use the convergence criterion $\epsilon = 10^{-3}$.

The simple iterative scheme outlined in Section 2.2.3 struggles to converge for realistic atmospheres with scattering. In the *Bifrost* model atmosphere, the smallest photon destruction probability is on the order 10^{-12}: the two-level atom will never converge in practice.

Instead of developing a more advanced Λ-iteration scheme with operator splitting to solve this problem, I modify the model atom to reduce the amount of scattering—the naive Λ-iteration algorithm is kept for simplicity. Scattering is reduced by multiplying the collisional rates C by a large factor, increasing the photon destruction probabilities ε_λ. This factor is sufficiently large to modify the smallest photon destruction probabilities up to the order 10^{-1}. In my calculations, the smallest photon destruction probabilities were between 0.08 and 0.1.

Chapter 4

Results

To build confidence in the irregular grid radiative transfer, I performed simple tests—before calculating the two-level atom. The irregular ray tracing algorithm was tested with the searchlight beam test and compared with the standard short characteristics ray tracing. Additionally, I tested the interpolation and sampling methods that constructed the irregular Voronoi grids. This last test was performed in LTE by comparing continuum calculations in an irregular grid with the Cartesian counterpart.

These tests validate all the algorithms involved in the irregular grid, ensuring the viability of simulating radiative on irregular grids. Passing the tests proves the ability to correctly propagate intensity through a medium and conserve information when mapping quantities to and from an irregular grid. After these tests, the main challenge in this thesis was to synthesise a spectral line in NLTE from the irregular grid.

4.1 Searchlight beam test

The first test I implemented is a straightforward experiment to validate ray tracing methods. The searchlight beam test establishes the ability to propagate radiation in an empty medium, similarly to pointing a flashlight through an empty box. In this test, we place an ingoing beam at one of the domain boundaries and measure the outgoing beam at the other boundary.

I set up a box with dimensions $1 \times 1 \times 1$ m^3 and populated it with 51^3 grid points. The irregular grid was constructed with sites drawn at random to ensure a similar density of sites throughout the box. If the sites were drawn from, e.g. the mass density in the *Bifrost* atmosphere, the grid would be much coarser on the top, making it poorly adapted for the searchlight beam test. The box's interior was assumed to be a perfect vacuum, making it completely transparent to radiation and not contributing any intensity to the beam. Thus, the source function and extinction coefficient were zero—$S_\lambda = 0$ kW m^{-2} nm^{-1} sr^{-1} and $\alpha_\lambda = 0$ m^{-1}. The ingoing intensity was set to be $I_{\text{beam}} = 1$ kW m^{-2} nm^{-1} sr^{-1}, constituting a beam with a radius of 0.2 m.

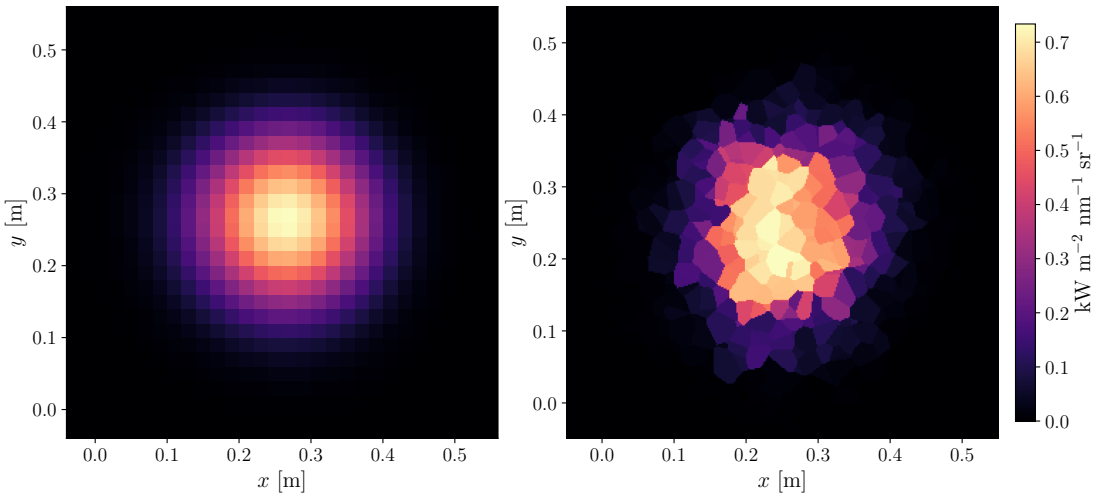

(a) Heatmaps of the searchlight beam test, performed in a regular geometry on the left side, and an irregular geometry on the right side.

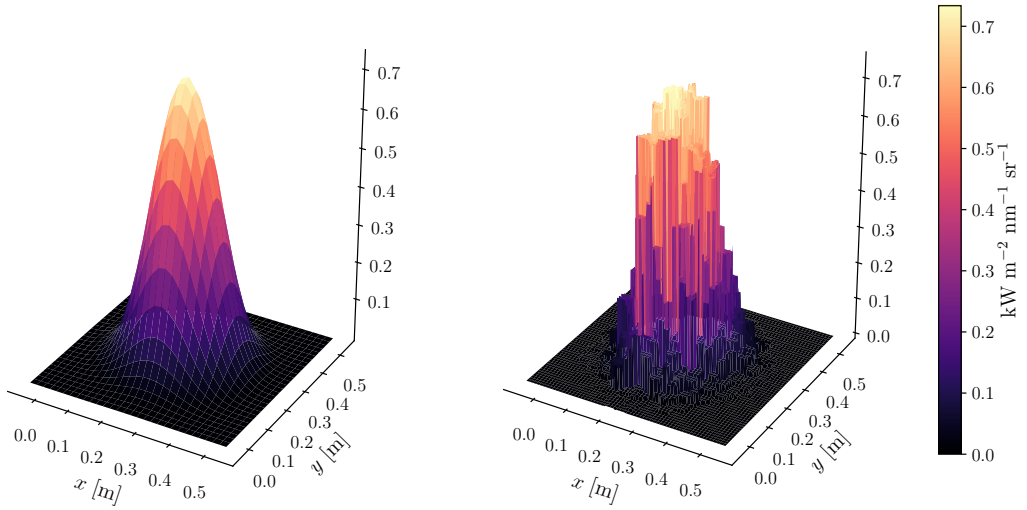

(b) Surface plots of the searchlight beam test, performed in a regular geometry on the left side, and an irregular geometry on the right side.

Figure 4.1: Searchlight beam test in a 1 m × 1 m × 1 m box with 51^3 grid points for regular and irregular ray tracing methods. The irregular grid was constructed with sites drawn from a uniform distribution. The beam was sent in with a radius of 0.2 m, and slanted at $\theta = 20°$, giving an inclination at approximately $\mu \approx 0.94$. In the *Top panel* we can see a comparison between the two methods displayed in heatmaps, while the *bottom* panel shows the comparison as surface plots.

The beam was directed from either the top or the bottom of the domain for several angles of incidence. For shallow rays—here taken as rays with an angle far away from the z-axis—the short characteristics method suffered from diffusion. While short characteristics on the regular grid managed to conserve the total flux to the other side of the domain, the intensity was spread from the original beam. The irregular grid ray tracing also handled shallow rays poorly, losing some flux through the box for rays $>\approx 45\,^{\circ}$. For less inclined rays with $\theta < 45^{\circ}$ away from the z-axis, the Delaunay ray tracing delivered results comparable to the short characteristics method on the regular grid.

The searchlight beam behaved as expected on the regular grid. For very inclined rays, the beam showed ample amounts of diffusion, but for more horizontal rays, the beam held together. The left plots of Figures 4.1a and 4.1b show the outgoing intensity of a beam slanted 20° away from the horizontal axis (inclination of $\mu = 0.94$). The left surface plot in Figure 4.1b compares well with figure 3 in Hayek et al. (2010). The ray tracing algorithm on the irregular grid also produced good results at the same inclination, as shown in the right parts of Figures 4.1a and 4.1b. Here, the outgoing intensity is comparable to the beam calculated on the regular grid. Both methods have outgoing intensities peak at approximately the same value. The Delaunay ray tracing method did not produce more diffusion than the short characteristics with a linear interpolation.

Using the searchlight beam test on the twelve ray quadrature (given in Štěpán et al., 2020; Jaume Bestard et al., 2021), I tracked the time usage in both ray tracing methods. For the same 51^3 grid, the Delaunay ray tracing method used 22.60 seconds, averaging at 1.88 seconds per solid angle. The short characteristics method was faster, using 2.31 seconds in total and averaging at 0.19 seconds per solid angle. This is almost a factor ten faster than the irregular grid ray tracing. However, when synthesising spectral lines, the ray tracing only constitutes a part of the actual time usage. The total time to synthesise spectral lines depends on multiple factors, including convergence.

4.2 Radiative transfer on irregular grids in LTE

Moving on, I used the *Bifrost* atmosphere to calculate radiative transfer. My first approach was to test the irregular grid algorithms in LTE, where the source function and populations were known everywhere. There was no need to find the source function iteratively, meaning that this test was quick to complete. The test consists of constructing an irregular grid, interpolating quantities to this grid, and then convert all quantities back to a regular grid to calculate the outgoing intensity. This test tells us whether the construction of the irregular grid conserves quantities important for radiative transfer. By sampling irregular grids according to different quantities, we will also get indications of regions important for the formation of radiation.

In this investigation, the source function was initialised by Equation (2.25). Since I calculated the continuum extinction of the hydrogen atom, I needed the atomic

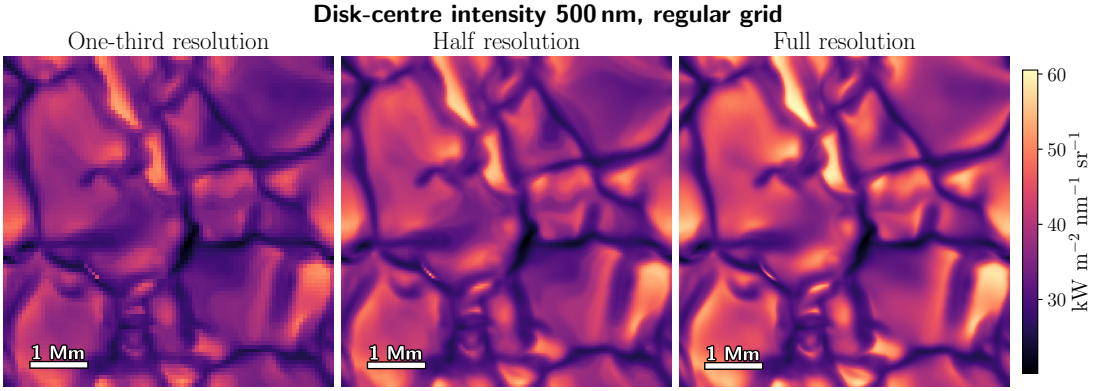

Figure 4.2: Disk-centre continuum intensity calculated from LTE in a regular geometry. Atmospheric parameters are that of the *Bifrost atmosphere*. The plots display the influence different resolutions of the atmosphere file have on the disk-centre intensity at 500 nm.

populations (a major contributor to the continuum extinction is the H^- ion). The atomic populations of hydrogen were computed with the Saha-Boltzmann statistics given in Equations (2.26)-(2.28). The continuum extinction coefficient was calculated with the `Transparency.jl` package, using the continuum processes described before Equation (3.12).

When the irregular grids were constructed, the extinction coefficient and source function were calculated for all sites in LTE. Then, the grids were converted back to a regular geometry by interpolating the source function and extinction coefficient onto a Cartesian grid. It is on these regular grids that the final radiation field was calculated. I computed the outgoing intensity at the wavelength 500 nm (dubbed λ_{500}) with zero inclination (we observe the atmosphere at disk-centre). I also calculated the LTE intensity on the original *Bifrost* atmospheric model to compare the results from the irregular grid construction. The outgoing intensity from the regular grid was calculated at three different resolutions of the model atmosphere: full resolution, half resolution, and one-third resolution. The full resolution model had 28 million grid points; the half resolution used every second point along each axis and had 3.5 million grid points; the one-third resolution model used every third point along each axis and had approximately one million grid points. Figure 4.2 shows intensity maps calculated from the regular grids. Here, we can see how higher resolutions reveal more resolved details. An interesting feature that we can observe is the magnetic brightening in the intergranular lane above the lower left corner. This feature coincides with the magnetic field at the surface, seen in Figure 3.1.

I used multiple sampling methods to construct the irregular grids. In this test, three are given special attention: drawing sites from the uniform distribution U, the vertical temperature gradient $\mathrm{d}T/\mathrm{d}z$, and the extinction coefficient α_{500}. I used trilinear

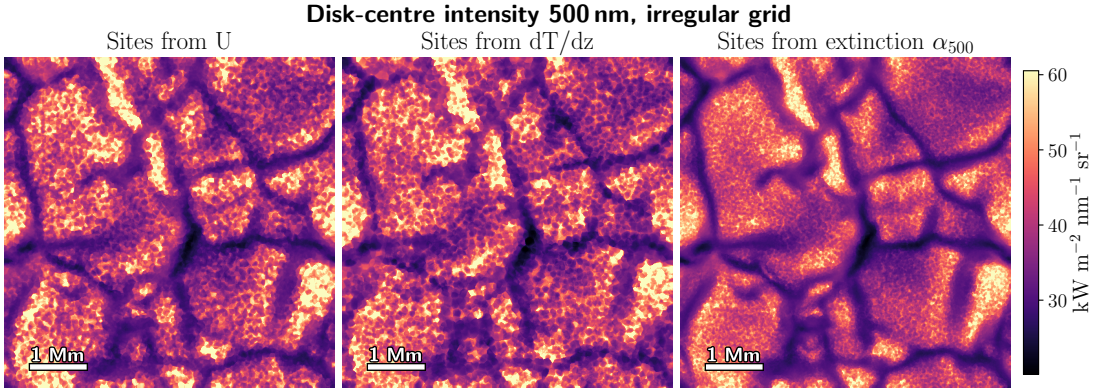

(a) Disk-centre intensity calculated from irregular grids with 500 000 sites sampled according to different distributions.

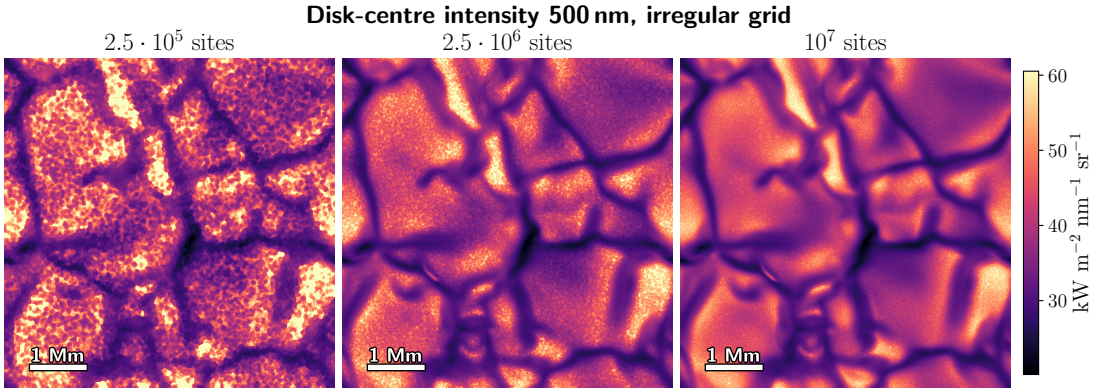

(b) Disk-centre intensity calculated from irregular grids constructed from continuum extinction α_{500} with different resolutions.

Figure 4.3: Disk-centre continuum intensity calculated from LTE in an irregular geometry. Atmospheric parameters are those of the *Bifrost* atmosphere. The *top panel* shows intensities calculated with 500 000 sites drawn from different sampling methods to construct the irregular grid. Finally, the *bottom panel* shows how different resolutions in the irregular grid influence the outgoing intensity. All irregular grids are constructed by drawing sites from the distribution reflecting the continuum extinction at 500 nm.

interpolation to adapt the *Bifrost* model atmosphere to irregular grids. Converting back to a regular grid, I used nearest neighbour interpolation. Although this is the simplest interpolation method, it reproduced the same results as the inverse distance weighting. The converted grid was given twice the resolution of the original grid—$(n_x = 512, n_y = 512, n_z = 860)$—to capture regions with a high density of sites.

I investigated how different sampling methods and number of sites in the irregular grids affected results. Grid points sampled from the extinction coefficient gave the best results for a low number of sites. Both the grids sampled from the uniform distribution and $\mathrm{d}T/\mathrm{d}z$ showed significant amounts of noise and failed to describe small-scale features of the outgoing intensity. A comparison of the outgoing intensity at disk-centre is presented in Figure 4.3a. For these calculations, I sampled one million sites to the irregular grid, a number much smaller than the number of grid points of the original atmosphere file (which is 28 million). Nonetheless, the grid sampled from extinction displayed similarities to the regular grids Figure 4.2.

The low resolution calculations were strongly affected by noise. By increasing the number of sites, this effect dissipated. As exemplified in Figure 4.3b, the noise dissipation becomes apparent. Here we can see that an increase in the number of sites produces results closer to those given with the full resolution grid in Figure 4.2. $250,000$ sites was not enough grid points to give good results. With 2.5 million sites, the outgoing intensity still looks grainy, but the magnetic brightening is clearly seen. The brightening is better resolved than in the quarter resolution results from the regular grid in Figure 4.2. For ten million sites, disk-centre intensity results were accurately reproduced compared to the full resolution regular grid. These results were calculated from a grid with only about a third of the grid points compared to the full resolution model. However, the differences with the full resolution regular grid are minor.

This analysis emphasises three points that are vital for this project. Firstly, the construction of the irregular grid works; the interpolations to an irregular grid and back to a regular grid did not lose vital information for radiative transfer. Secondly, I have found that the sampling method has a large impact on the results. It is important to construct a grid that highlights the important regions in the atmosphere. The last point—the most promising for this project—is that it is possible to reproduce intensity from irregular grids with fewer grid points accurately.

4.3 Radiative transfer on irregular grids in NLTE

Finally, I synthesised the two-level atom's spectral line in NLTE with the Λ-iteration algorithm. The spectral line was calculated from the *Bifrost* model atmosphere, that is adapted to irregular grids. The two-level atomic line is equivalent to the Ly-α line, but the model atom had artificially increased collisional rates to facilitate convergence.

The spectral line was calculated with 90 wavelength points distributed over the bound-bound and two bound-free processes. With 50 wavelength points, the bound-bound

transition was calculated assuming CRD. Both ionisation stages were calculated with 20 wavelength points each. Iterating over many wavelength points with the full resolution of the MHD simulation involved extensive computation, which was not viable for the analyses in this thesis. In order to reduce computation time, I did not use the full resolution. Instead, I used lower resolutions to synthesise the line.

I started by modelling the atom on three different resolutions of the regular grid: every second point (half resolution with 3.5 million grid points), every third point (one-third resolution with one million grid points), and every fourth point (quarter resolution with 500,000 grid points) of the original *Bifrost* atmosphere. Across the resolutions, the results varied significantly. I calculated the disk-centre intensity and found that lower resolution simulations gave stronger lines. This is presented in Figure 4.4. Here, we see that the line core is stronger in almost every pixel for lower resolution simulations. It is also apparent that small-scale features get smeared out or disappear in the coarser grids.

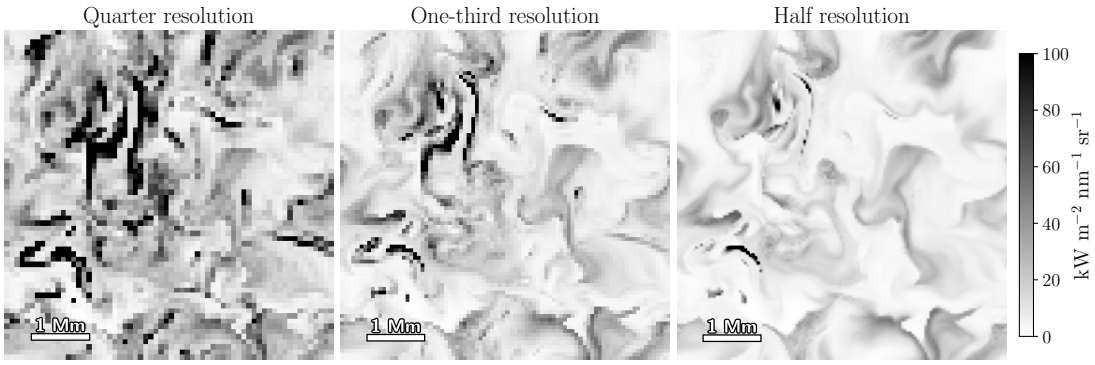

Figure 4.4: Disk-centre intensity at line centre calculated on regular grids with different resolutions. Atmospheric parameters are that of the *Bifrost atmosphere*.

With higher resolution, the source function required more iterations to converge, consistent with Štěpán et al. (2022) who note that convergence speed is proportional to N^4. The quarter, one-third, and half resolution grids converged in 78, 87, and 92 iterations.

Moving onward, I wished to reproduce results similar to the regular grid by solving the NLTE two-level atom problem on irregular grids. To find an optimised grid for the problem, I constructed multiple grids sampled from different distributions. The grids were constructed to reflect the density of the following quantities:

1. The continuum extinction at line centre, α_0^c.
2. Ionised hydrogen density in LTE, $N_{\mathrm{H\,II}}^{\mathrm{LTE}}$.
3. The photon destruction probability, ε.
4. Total hydrogen density, N_{H}.

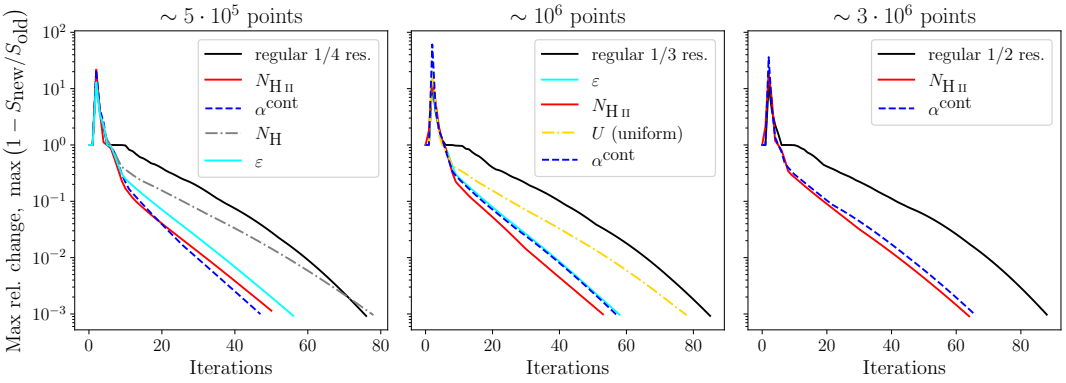

Figure 4.5: Λ iteration convergence for a selection of simulations. Here, all simulations on the regular grid are plotted with black lines, while irregular grid simulations are plotted in color lines. Results are grouped together by resolution: for the regular grids the half resolution grid has approximately $3 \cdot 10^6$ points, one-third has $\sim 10^6$ points, while the quarter grid has around $5 \cdot 10^5$ points.

5. A uniform distribution, U.

For the purpose of comparing results at different resolutions, grids were constructed with a varying number of sites. Due to the time consumption of the calculations, I used a maximum of three million sites in the irregular grids. This number is comparable to sampling half of the points in every direction of the original atmosphere; the half resolution atmosphere had 3.5 million grid points.

I found an accelerated convergence on several of the irregular grids. This speedup was found in the grids constructed according to continuum extinction, ionised hydrogen density, and photon destruction probability. Grids that were sampled according to the total hydrogen density and uniform distribution needed many iterations to converge, performing similarly to the regular grids. Figure 4.5 displays the convergence for these simulations. In the figure, all relative changes start at one due to the initialisation of the source function. In the first iteration, $S_{\text{new}} = B_\lambda(T)$ and $S_{\text{old}} = 0$ kW m^{-2} nm^{-1} sr^{-1}. The figure displays many irregular grids converging faster at all resolutions. The total time usage of the calculations did not see the same improvement: with the current implementation, the irregular grids were six times slower than the regular grids per iteration.

To observe which grids gave better results, I constructed grids with one million sites from the different sampling methods. These results are presented in Figure 4.6. No grid gave results as good as the quarter resolution regular grid with one million grid points in Figure 4.4. Nevertheless, we can see differences in the plots indicating that some sampling methods gave better results than others. For instance, the grids sampled from the photon destruction probability and ionised hydrogen density are lighter, making

the total flux smaller. They are more similar to the quarter resolution result from the regular grid.

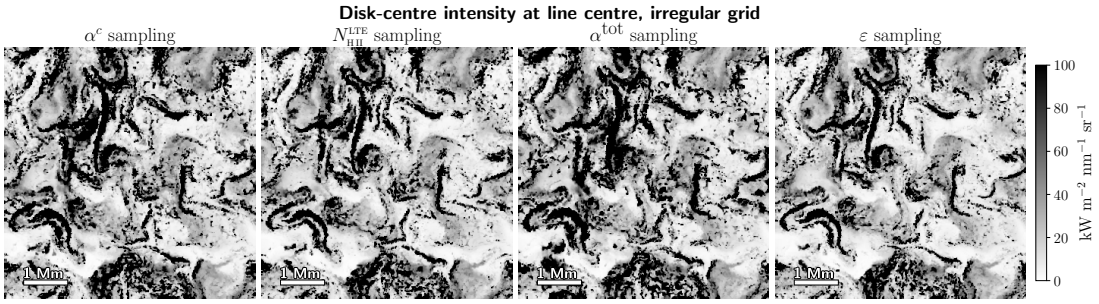

Figure 4.6: Disk-centre intensity at line centre computed with several irregular grids. The irregular grids were sampled from different distributions with one million sites each.

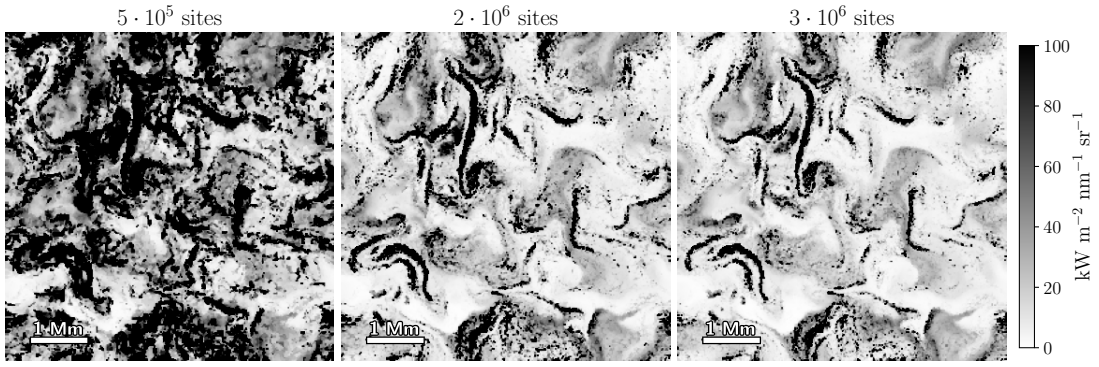

Figure 4.7: Disk-centre intensity at line centre computed with an irregular grid at different resolutions. Here, the irregular grids are sampled from the continuum extinction.

The results showed a large amount of noise in the irregular grids with one million sites. This noise hampers details in the outgoing intensity. To find out why there is noise in the results, we can consider the sampling method of the irregular grids. Since the sampling is done with a stochastic method, it produces noise when the number of sites is low. We expect noise to decrease when we sample more sites on the grids. To see why we need more points in the irregular grids, we can compare the quarter resolution results from Figure 4.4 with the irregular grids' results. The quarter resolution intensity shares more similarities with the irregular grids than the one-third and half resolution grids. High resolution is needed to produce accurate results for both regular and irregular grids.

While the convergence speed of the two-level atom improved in the irregular grids, the results contained noise, apparent when the outgoing intensity was calculated. This noise was a remnant of the stochastic sampling of the grid. By sampling more sites in the irregular grids, I expected better results. In Figure 4.7, I calculated the line with

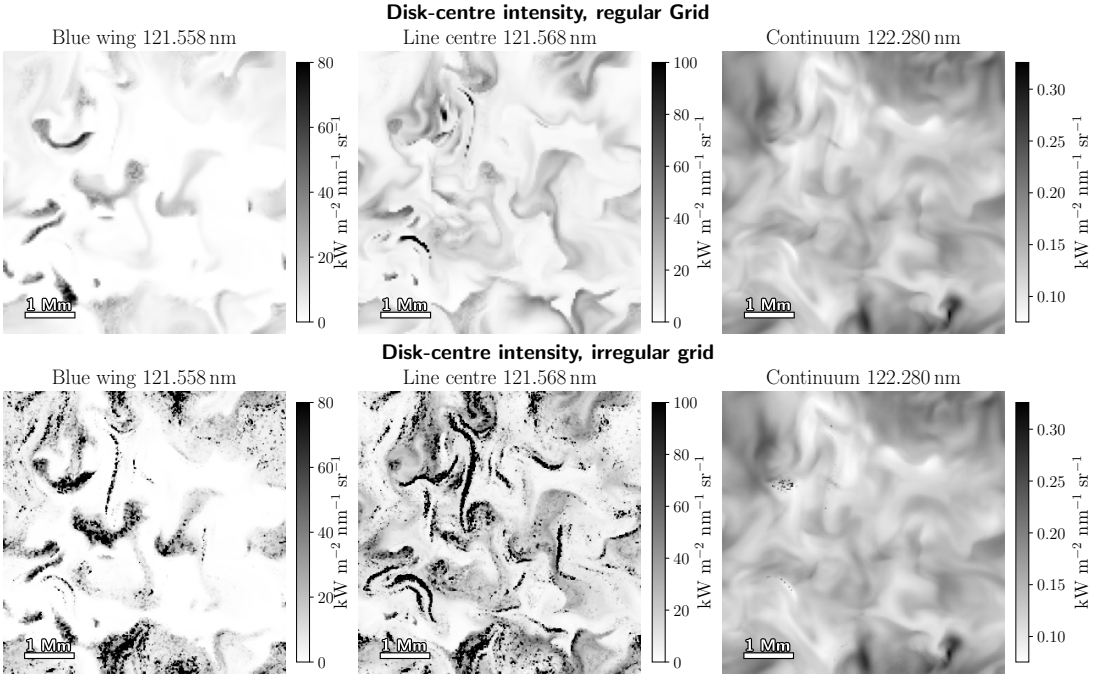

Figure 4.8: Disk-centre intensity for three different wavelengths calculated with the half-resolution regular grid (top panels), and with an irregular grid with three million sites sampled from the ionised hydrogen density (bottom panels). The Blue wing is Doppler shifted $-27\,\mathrm{km\,s^{-1}}$ from the line centre.

different resolutions in the irregular grids. The irregular grids were sampled from the continuum extinction coefficient, a distribution that favours grid points in the lower parts of the atmosphere. Here, we can see how the outgoing intensity at the line core varies when the resolution in the grid increases. These plots show an improvement with higher resolution. For grids with more sites, we can recognise smaller features in the outgoing intensity. With three million sites, the outgoing intensity shares many similarities with the one-third resolution regular grid in Figure 4.7.

Differences in the line core at disk-centre have been investigated; the whole line is yet to be discussed. Figure 4.8 compares the spectral line synthesised from an irregular grid (constructed with 3 million sites sampled from the LTE ionised hydrogen density) with the regular method at the line centre, in the blue wing, and the continuum. It is possible to recognise features in the line centre across the different methods. The line wing compares better than the line centre, being more similar across the irregular and regular grid. The continuum intensities are almost identical. There are merely a few bright spots in the intensity from the irregular grid, which are not reproduced from the regular grid. The intensity contains noise (seen as dark spots on the intensity map), which makes it apparent that the irregular grid needs more sites.

A more representative figure of the spectral line is presented in Figure 4.9, where the

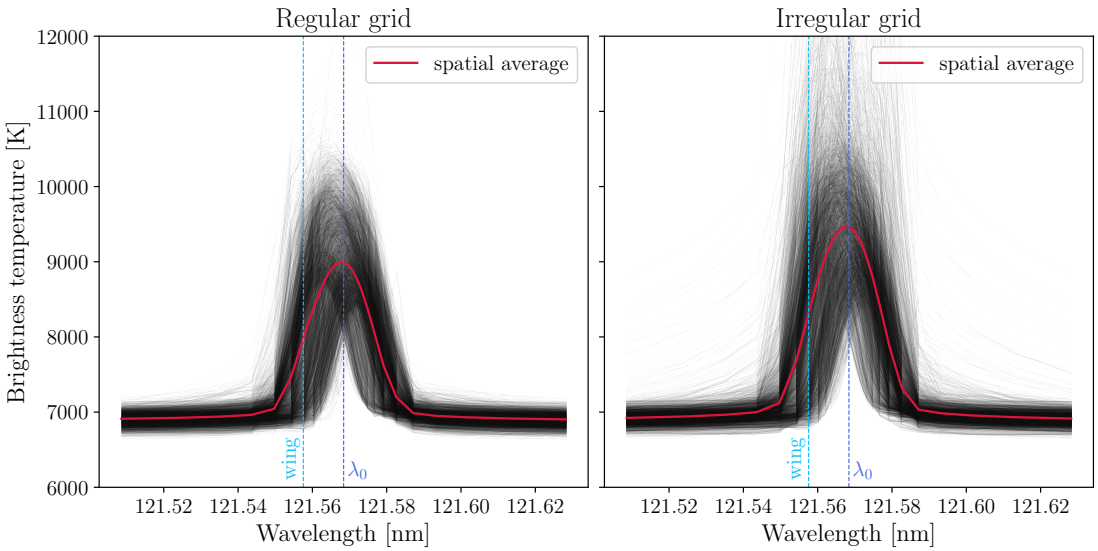

Figure 4.9: Individual line profiles for disk-centre intensity calculated from the half resolution regular grid and an irregular grid with three million sites sampled from the ionised hydrogen density. Intensity is converted to brightness temperature, by inverting the Planck function. Every black line corresponds to the brightness temperature from a column in the atmosphere. The spatial average over all columns is represented by the red line. Dashed blue lines indicate wavelength positions of the blue wing at 121.558 nm (or -27 km s^{-1}) and line centre λ_0 at 121.568 nm.

intensity is converted to brightness temperature. This figure displays the spectral line versus wavelength for the columns in the atmosphere, making it easier to see how the methods differ over wavelength. Differences are more extensive in the line core but small in the wings. The spatial averages plotted in the figure emphasise this. While the irregular grid produced some outlying lines in the wings, the bulk of the lines lies close to the regular grid spectral lines. The spatial average from the irregular grid is significantly stronger in the line core.

A pertinent question to ask now is: can we construct a grid with few sites and at the same time produce accurate results? This is a matter of finding locations in the atmosphere that require a high density of sites—i.e. regions sensitive to line formation. We can see where the density of sites should be high by investigating where the line forms. Since most radiation forms at optical depth $\tau_\lambda = 1$—per Eq. (2.4)—this region is important to emphasise in the grid. The height of formation is found as $h(\tau = 1)$. I calculate the height of formation for disk-centre intensity and a location in the line wing, and compare these heights with the density of grid points versus height in the regular and irregular grids with three million sites. Histograms showing these statistics are seen in Figure 4.10. We can see that the line centre is formed higher in the atmosphere, with the line wing formation taking place deeper down in the atmosphere. The mean height of formation is 2.7 Mm in the line centre and 2.3 Mm in the blue wing. The

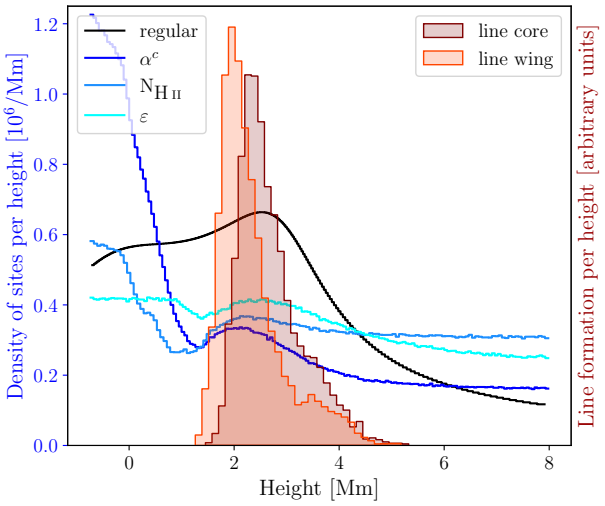

Figure 4.10: Histograms comparing features of irregular grids, and height of formation in the line. The black and blue lines (left axis) portray the density of sites versus height for the half resolution regular grid and irregular grids constructed from three different sampling methods. These grids are sampled with three million sites. The red histograms (right axis) show the density of line formation per height for the line centre and line wing (where $\tau = 1$). Line wing is at -27 km s^{-1}.

grid construction methods used in this thesis do not emphasise these high regions of the atmosphere. This issue became apparent later when there was not enough time to conduct new analyses with more apt sampling methods capturing these regions.

The histograms in Figure 4.10 depict the heights that deserve a higher density of grid points to synthesise vertical radiation. In three dimensions, the vertical direction is "half the truth"—we should consider every direction to identify regions that need extra attention. Inclined rays travel farther through the atmosphere per height gain, and consequently, this radiation forms higher. For rays with an inclination of $\mu = 0.7$, the mean height of formation was 3.0 Mm in the line core, and 2.6 Mm in the blue wing. This reasoning builds under the assumption that an ideal grid should emphasise even higher regions than those accentuated with the line formation regions in Figure 4.10.

Expanding the analysis of which regions need better resolution, I compared the converged source functions of the regular and irregular grids. By calculating the source functions' relative difference between the two methods, we can observe where the source functions converged towards the same value and where they differed. A small relative difference should indicate that the relevant region had sufficient resolution. A high relative difference is indicative of the opposite. The source functions' maximum relative difference over wavelength is presented in Figure 4.11. Here, every column of the atmosphere is compared and plotted per height. The figure shows that the very bottom and top regions of the atmosphere have a small relative difference. In the middle regions (from the surface at 0 Mm until around 3.5 Mm), the relative difference is high. Some of this difference came from interpolating to and from the irregular grid; however, this does not explain the sharp variations through the atmosphere. The irregular grids need more sites in the middle regions to mitigate this difference.

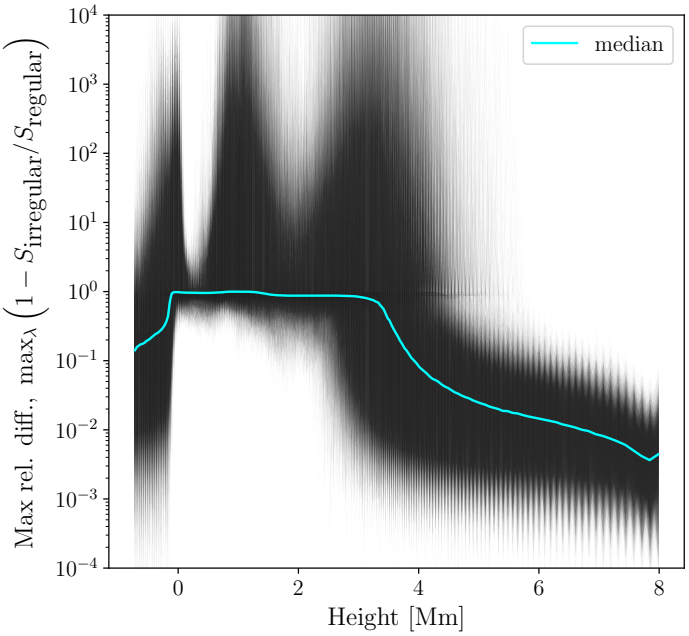

Figure 4.11: Maximum relative difference between source functions calculated on the regular with half resolution and irregular grid (sampled with three million sites from ionised hydrogen density). Every line corresponds to the difference in a column of the atmosphere. The median of the maximum relative difference is shown with the cyan line.

Chapter 5

Conclusions and future work

NLTE radiative transfer calculations are essential to accurately reproduce various spectral lines observed in the solar spectrum. Details in these spectral lines are often inherently three-dimensional. Spectral synthesis in 3D has been met with high computational complexity and slow convergence. Nevertheless, the evolution of better optics for solar observations requires high resolution 3D simulations to uncover the mechanisms that develop small-scale details in spectra. Therefore, improved methods for 3D radiative transfer calculations on high resolution simulations are key for advancing our understanding of the Sun.

This thesis develops a new method to calculate radiative transfer on irregular grids. With the irregular grid, I could vary the density of grid points through the computational domain. Thus, highly variable regions contributing sharp changes to radiative transfer could be resolved with more grid points, while monotonous regions were less resolved. The irregular grid can resolve important details without acquiring high computational complexity.

Calculating radiative transfer on an irregular grid required a ray tracing algorithm different from the traditional long and short characteristics applied to Cartesian grids. To traverse irregular grids, I constructed a Voronoi diagram of the grid points and traced rays along the Delaunay lines of this diagram. This ray tracing method performed satisfactory in the searchlight beam test and did not produce more diffusion than short characteristics with linear interpolation.

An uncertainty that arose during my work was related to the construction of the irregular grid: is an irregular grid capable of conserving important information for radiative transfer? I interpolated a *Bifrost* atmospheric model—where quantities were defined on a Cartesian grid—onto an irregular grid. By constructing the atmospheric model in LTE, I found that it is possible to construct irregular grids capable of capturing the essential components for radiative transfer. It was possible to accurately reproduce radiative transfer calculations in LTE with an irregular grid having fewer grid points

than the regular grid counterpart.

Improving convergence of Λ iterations is important in NLTE radiative transfer. To find out whether irregular grids can accelerate convergence, I calculated a two-level atom on a quiet sun *Bifrost* simulation in NLTE. The key assumptions made in the model were:

- Including the ground and first excited state of the hydrogen atom, plus continuum.
- Complete redistribution of the line profile.
- Artificially increased collisional rates to facilitate convergence.
- Reducing the resolution of the model atmosphere to keep the computational complexity manageable.

It was found that the irregular grids only partly managed to reproduce the spectral line at the reduced resolution. Results also depended on the construction of the irregular grid. For the grids I have explored in this thesis, none seemed to place enough grid points in the upper parts of the atmosphere. Nonetheless, several irregular grids gave an accelerated convergence compared to the Cartesian grid. For the grid samplings that gave faster convergence, the speedup was current at multiple grid resolutions at almost a factor of two. This speedup across resolutions implies that an accelerated convergence should be expected for higher resolution calculations.

Future exploration of radiative transfer on irregular grids should include grid samplings that better accentuate the regions most relevant for line formation. A good starting point can be to average the total extinction over the solid angles of the quadrature used to compute the mean intensity, then construct an irregular grid to reflect this quantity.

Developments to the code are needed to further the analysis. Firstly, extending the code with MPI parallelisation and domain decomposition would accommodate higher resolution calculations. A second important inclusion is to incorporate operator splitting. Operator splitting would enable NLTE calculations without artificially increasing collisional rates. Optimising the Delaunay ray tracing is possible. The horizontal boundary conditions are currently treated with `if` tests, involving additional calculations for every site. Incorporating horizontal boundary information in the neighbour matrix will speedup the Delaunay ray tracing algorithm.

Reducing noise in the irregular grids is also possible. To give a fairer distribution of grid points in the domain, one could demand that grid points can only be so close to each other. Upon the construction of the irregular grid, we can check the distances to all other sites before sampling a new site. This method would ensure that grid points are not placed too close, and reduce noise in the grids.

The conclusions from this work can be summarised with these key takeaways:

- Delaunay ray tracing through irregular grids transports radiation accurately.

- Constructing an optimised grid conserves quantities important for radiative transfer.
- Irregular grids can accurately synthesise radiation with fewer grid points than a regular grid.
- Optimised grids accelerate the source function's convergence by almost a factor of two.
- To accurately reproduce spectral lines, irregular grids need higher resolutions. The current maximal resolution has three million grid points.

Bibliography

Bates, D. R. 1952, MNRAS, 112, 40, doi: 10.1093/mnras/112.1.40

Bezanson, J., Edelman, A., Karpinski, S., & Shah, V. B. 2017, SIAM Review, 59, 65, doi: 10.1137/141000671

Bjørgen, J. P., & Leenaarts, J. 2017, A&A, 599, A118, doi: 10.1051/0004-6361/201630237

Brinch, C., & Hogerheijde, M. R. 2010, A&A, 523, A25, doi: 10.1051/0004-6361/201015333

Camps, P., Baes, M., & Saftly, W. 2013, A&A, 560, A35, doi: 10.1051/0004-6361/201322281

Cannon, C. J. 1973, ApJ, 185, 621, doi: 10.1086/152442

Carlson, B. G. 1955, Solution of the transport equation by Sn approximations, Technical Report LA-1891, Los Alamos National Lab, doi: 10.2172/4376236

—. 1963, Methods in computational physics, Vol. 1 (New York: Academic Press)

Carlsson, M. 1986, Uppsala Astronomical Observatory Reports, 33

Carlsson, M., & Stein, R. F. 1992, ApJ, 397, L59, doi: 10.1086/186544

Crosbie, A. L., & Linsenbardt, T. L. 1978, J. Quant. Spectrosc. Radiative Transfer, 19, 257, doi: 10.1016/0022-4073(78)90061-4

Dalgarno. 1962, Tech. Rep. 62-28-A, Geophysics Corp. of America

de la Cruz Rodríguez, J., & Piskunov, N. 2013, ApJ, 764, 33, doi: 10.1088/0004-637X/764/1/33

de Vicente, A., del Pino Alemán, T., & Trujillo Bueno, J. 2021, ApJ, 912, 63, doi: 10.3847/1538-4357/abec6b

Delaunay, B. 1934, Bulletin de l'Académie des Sciences de l'URSS. Classe des sciences mathématiques et naturelles, 7, 793

Dirichlet, L. 1850, J. für Reine Angew. Math., 1850, 209

Dorfi, E. A., & Drury, L. O. 1987, Journal of Computational Physics, 69, 175, doi: 10.1016/0021-9991(87)90161-6

Fontenla, J. M., Avrett, E. H., & Loeser, R. 1993, ApJ, 406, 319, doi: 10.1086/172443

Geltman, S. 1962, ApJ, 136, 935, doi: 10.1086/147447

Gray, D. F. 2005, The Observation and Analysis of Stellar Photospheres, 3rd edn. (Cambridge University Press), doi: 10.1017/CBO9781316036570

Gudiksen, B. V., Carlsson, M., Hansteen, V. H., et al. 2011, A&A, 531, A154, doi: 10.1051/0004-6361/201116520

Hansen, I. R. 2021, Master's thesis, University of Oslo

Hayek, W., Asplund, M., Carlsson, M., et al. 2010, A&A, 517, A49, doi: 10.1051/0004-6361/201014210

Janett, G. 2019, A&A, 622, A162, doi: 10.1051/0004-6361/201833984

Janett, G., Steiner, O., & Belluzzi, L. 2018, ApJ, 865, 16, doi: 10.3847/1538-4357/aad4a4

Jaume Bestard, J., Štěpán, J., & Trujillo Bueno, J. 2021, A&A, 645, A101, doi: 10.1051/0004-6361/202039424

Jones, H. P. 1973, ApJ, 185, 183, doi: 10.1086/152407

Jones, H. P., & Skumanich, A. 1973, ApJ, 185, 167, doi: 10.1086/152406

Keller, H. B., & Wendroff, B. 1957, Commun. Pure Appl. Anal., 10, 567, doi: https://doi.org/10.1002/cpa.3160100407

Kramida, A., Yu. Ralchenko, Reader, J., & and NIST ASD Team. 2021, NIST Atomic Spectra Database. National Institute of Standards and Technology, Gaithersburg, MD., doi: https://dx.doi.org/10.18434/T4W30F

Kunasz, P., & Auer, L. H. 1988, J. Quant. Spectrosc. Radiative Transfer, 39, 67, doi: 10.1016/0022-4073(88)90021-0

Leenaarts, J., Carlsson, M., & Rouppe van der Voort, L. 2012, ApJ, 749, 136, doi: 10.1088/0004-637X/749/2/136

Mihalas, D. 1978, Stellar atmospheres, 2nd edn., A Series of books in astronomy and astrophysics (San Francisco: Freeman)

Olson, G. L., Auer, L. H., & Buchler, J. R. 1986, J. Quant. Spectrosc. Radiative Transfer, 35, 431, doi: 10.1016/0022-4073(86)90030-0

Paardekooper, J. P., Kruip, C. J. H., & Icke, V. 2010, A&A, 515, A79, doi: 10.1051/0004-6361/200913821

Pereira, T. M. D. 2021, tiagopereira/Transparency.jl: v0.1.7, v0.1.7, Zenodo, doi: 10.5281/zenodo.5667017

Rees, D. E., Murphy, G. A., & Durrant, C. J. 1989, ApJ, 339, 1093, doi: 10.1086/167364

Rutten, R. J. 2003, Radiative Transfer in Stellar Atmospheres, Utrecht University lecture notes, 8th edition

—. 2019, Introduction to Astrophysical Radiative Transfer

Rybicki, G. B., & Hummer, D. G. 1991, A&A, 245, 171

Rycroft, C. H. 2009, Chaos, 19, 041111, doi: 10.1063/1.3215722

Scharmer, G. B. 1981, ApJ, 249, 720, doi: 10.1086/159333

Stein, R. F., & Nordlund, Å. 1998, ApJ, 499, 914, doi: 10.1086/305678

Steiner, O., Züger, F., & Belluzzi, L. 2016, A&A, 586, A42, doi: 10.1051/0004-6361/201527158

Stilley, J. L., & Callaway, J. 1970, ApJ, 160, 245, doi: 10.1086/150423

Udnæs, E. 2022, meudnaes/VoronoiRT: First version, v1.0.0, Zenodo, doi: 10.5281/zenodo.6528467

Uitenbroek, H. 2001, ApJ, 557, 389, doi: 10.1086/321659

van de Weygaert, R. 1994, A&A, 283, 361

Voronoi, G. 1908, J. für Reine Angew. Math., 1908, 198, doi: 10.1515/crll.1908.134.198

Štěpán, J., del Pino Alemán, T., & Trujillo Bueno, J. 2022, A&A, 659, A137, doi: 10.1051/0004-6361/202142079

Štěpán, J., Jaume Bestard, J., & Trujillo Bueno, J. 2020, A&A, 636, A24, doi: 10.1051/0004-6361/202037566

Witze, A. 2020, World's most powerful solar telescope is up and running, doi: 10.1038/d41586-020-00224-z